The Astrophysical Journal, 984:50 (16pp), 2025 May 1 https://doi.org/10.3847/1538-4357/adc2f7

Comparative Analysis of Hall Effect Implementations in Hall Magnetohydrodynamics

Kazunari Iwasaki[1,2] and Kengo Tomida[3]
[1] Center for Computational Astrophysics, National Astronomical Observatory of Japan, 2-21-1 Osawa, Mitaka, Tokyo 181-8588, Japan; kazunari.iwasaki@nao.ac.jp
[2] Astronomical Science Program, The Graduate University for Advanced Studies (SOKENDAI), 2-21-1 Osawa, Mitaka, Tokyo 181-8588, Japan
[3] Astronomical Institute, Tohoku University, Sendai, Miyagi, 980-8578, Japan
Received 2025 February 7; revised 2025 March 18; accepted 2025 March 18; published 2025 April 24

Abstract

There is no standard numerical implementation of the Hall effect, which is one of the nonideal magnetohydrodynamic (MHD) effects. Numerical instability arises when a simple implementation is used, in which the Hall electric field is added to the electric field to update magnetic fields without further modifications to the numerical scheme. In this paper, several implementations proposed in the literature are compared to identify an approach that provides stable and accurate results. We consider two types of implementations of the Hall effect. One is a modified version of the Harten–Lax–van Leer method (HALL-HLL), in which the phase speeds of whistler waves are adopted as the signal speeds; the other involves adding a fourth-order hyper-resistivity to a Hall-MHD code. Based on an extensive series of test calculations, we find that hyper-resistivity yields more accurate results than HALL-HLL, particularly in problems where the whistler wave timescale is shorter than the timescales of the physical processes of interest. Through both von Neumann stability analysis and numerical experiments, an appropriate coefficient for the hyper-resistivity is determined.

Unified Astronomy Thesaurus concepts: Computational methods (1965); Magnetohydrodynamical simulations (1966); Magnetic fields (994)

1. Introduction

The Hall effect is one of the nonideal magnetohydrodynamic (MHD) effects. It occurs in situations where electrons are coupled to magnetic fields, while ions are decoupled. The characteristics of the Hall effect differ between fully ionized and weakly ionized gases (B. P. Pandey & M. Wardle 2008).

An intriguing property of the Hall effect is that it modifies the dispersion relation of linear MHD waves, leading to the generation of whistler and ion-cyclotron waves. In the long-wavelength limit, these waves transition into Alfvén waves. The phase speed of whistler waves increases proportionally to the wavenumber, whereas that of ion-cyclotron waves remains constant at higher wavenumbers.

Numerically implementing the Hall effect presents significant challenges, unlike other nonideal MHD effects (ohmic resistivity and ambipolar diffusion), which are relatively simple to implement. One reason is that the Hall effect causes waves to be dispersive. In particular, as whistler waves with shorter wavelengths propagate faster, grid-scale disturbances in magnetic fields can become significant under certain conditions.

A simple implementation of the Hall effect involves adding the Hall electric field to the electric field to update the magnetic field without further modifications to the numerical scheme. S. A. E. G. Falle (2003) conducted a von Neumann stability analysis of such a naive implementation and found it to be unconditionally unstable when using a first-order explicit time integrator (forward-Euler integrator).

The stability of this simple implementation depends on the accuracy of the time integrator (M. W. Kunz & G. Lesur 2013). While third-order time integrators are conditionally stable, second-order time integrators may lead to numerical instability. G. Lesur et al. (2014) confirmed that a third-order Runge–Kutta (RK3) time integrator suppresses numerical instabilities in the nonlinear development of Hall-dominated magnetorotational instability using `SNOOPY`, an incompressible pseudo-spectral code. However, no studies have shown that the RK3 integrator, combined with a simple implementation, provides stable results when using Godunov-type schemes with constrained transport (CT) methods (C. R. Evans & J. F. Hawley 1988), which is a popular combination used in many MHD simulation codes, such as J. M. Stone et al. (2020; `Athena++`), S. Fromang et al. (2006; `RAMSES`), A. Mignone et al. (2007; `Pluto`), and D. C. Collins et al. (2010; `Enzo`).

Another issue with the simple implementation is that it does not provide numerical dissipation, because the Hall electric field is oriented perpendicular to the electric current. This lack of numerical dissipation causes serious problems in magnetic reconnection driven by the Hall effect (e.g., M. E. Mandt et al. 1994).

Several numerical methods have been proposed to suppress the numerical instabilities caused by the Hall effect. G. Tóth et al. (2008) and G. Lesur et al. (2014) suggested modifying the signal speeds in the Harten–Lax–van Leer (HLL; A. Harten et al. 1983) numerical fluxes by considering the phase speed of whistler waves to estimate the signal speeds of the two characteristics. This method is called HALL-HLL and is widely used in numerical simulations of star and planet formation (X.-N. Bai & J. M. Stone 2017; W. Béthune et al. 2017; P. Marchand et al. 2018). P. Marchand et al. (2019) proposed a modified HALL-HLL method to improve the conservation of angular momentum in collapsing dense molecular cloud cores.

Alternative approaches for modifying time integration methods have also been proposed. S. A. E. G. Falle (2003) demonstrated that an implicit method stabilizes Hall-MHD. Furthermore, G. Tóth et al. (2008) showed that an implicit Hall-MHD scheme is stable even without modifications to the

numerical fluxes. S. O'Sullivan & T. P. Downes (2006, 2007) found that the Hall-MHD stability is achieved when the magnetic field is updated using a dimensionally split method (also see X.-N. Bai 2014).

Another approach involves introducing artificial resistivity into the induction equation. For instance, hyper-resistivity is added to damp whistler waves with wavelengths comparable to the grid scale in numerical simulations of magnetic reconnection involving the Hall effect (e.g., J. Birn et al. 2001; Z. W. Ma & A. Bhattacharjee 2001; D. Viganò et al. 2021; L. Chacón & D. A. Knoll 2003). However, an appropriate choice of the hyper-resistivity coefficient has not been thoroughly examined. Recently, O. Zier et al. (2024) proposed a method in which the diffusion coefficient of ohmic resistivity is artificially increased to stabilize the schemes.

As mentioned earlier, various implementations of the Hall effect have been proposed in the literature. However, comprehensive comparisons of their stability and accuracy have not yet been conducted. In this paper, we compare the results of HALL-HLL (G. Lesur et al. 2014), a modified version of HALL-HLL (P. Marchand et al. 2019), and hyper-resistivity (J. Birn et al. 2001).

This paper is organized as follows: Section 2 reviews the basic properties of Hall-MHD and describes the implementations considered in this paper, while Section 3 presents numerical experiments. We conclude in Section 4.

2. Basic Properties of Hall-MHD and Its Numerical Implementations

2.1. Basic Equations

The basic equations of nonideal MHD are given by:

$$\frac{\partial \rho}{\partial t} + \frac{\partial \rho v_i}{\partial x_i} = 0, \tag{1}$$

$$\frac{\partial \rho v_i}{\partial t} + \frac{\partial}{\partial x_j}(\rho v_i v_j + \mathcal{T}_{ij}) = 0, \tag{2}$$

$$\frac{\partial E}{\partial t} + \frac{\partial}{\partial x_i}\{E v_i + \mathcal{T}_{ij} v_j + (\boldsymbol{E}_{\rm ni} \times \boldsymbol{B})_i\} = 0, \tag{3}$$

and

$$\frac{\partial \boldsymbol{B}}{\partial t} + \boldsymbol{\nabla} \times (-\boldsymbol{v} \times \boldsymbol{B} + \boldsymbol{E}_{\rm ni}) = 0, \tag{4}$$

where ρ is the density, $\boldsymbol{v}$ is the velocity, $\boldsymbol{B}$ is the magnetic field, P is the pressure, and $E = \rho \boldsymbol{v}^2/2 + P/(\gamma - 1) + \boldsymbol{B}^2/8\pi$ represents the total energy per unit volume. $\mathcal{T}$ denotes the stress tensor, given by

$$\mathcal{T}_{ij} = \left(P + \frac{B^2}{8\pi}\right)\delta_{ij} - \frac{B_i B_j}{4\pi}. \tag{5}$$

$\boldsymbol{E}_{\rm ni}$ represents the electric field resulting from nonideal MHD effects, expressed as

$$\boldsymbol{E}_{\rm ni} = \frac{4\pi}{c}\left(\eta_{\rm O}\boldsymbol{J} + \eta_{\rm H}\frac{\boldsymbol{J} \times \boldsymbol{B}}{|\boldsymbol{B}|} + \eta_{\rm A}\boldsymbol{J}_\perp\right), \tag{6}$$

$\boldsymbol{J} = (c/4\pi)\boldsymbol{\nabla} \times \boldsymbol{B}$ is the electric current density, and $\boldsymbol{J}_\perp = \boldsymbol{J} - (\boldsymbol{J} \cdot \boldsymbol{B})/|\boldsymbol{B}|$ is the $\boldsymbol{J}$ components perpendicular to the local magnetic field direction. $\eta_{\rm O}$, $\eta_{\rm H}$, and $\eta_{\rm A}$ correspond to the diffusion coefficients for ohmic resistivity, the Hall effect, and ambipolar diffusion, respectively. In this study, ohmic resistivity and ambipolar diffusion are not considered, because the focus is on implementations that ensure stability and accuracy even with $\eta_{\rm O} = \eta_{\rm A} = 0$.

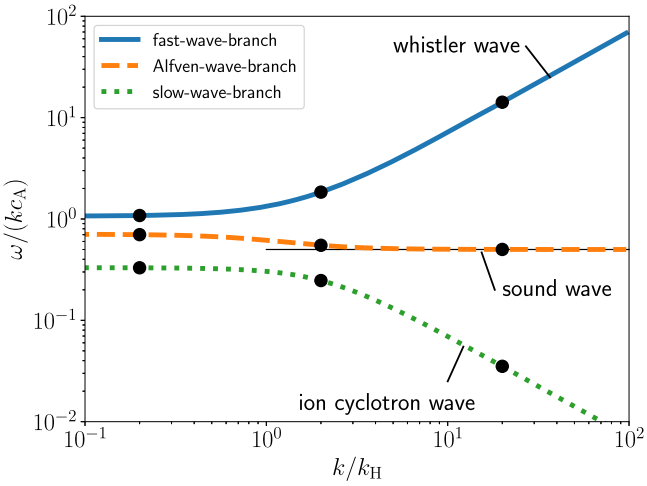

Figure 1. Phase speeds of the fast-wave branch, Alfvén-wave branch, and slow-wave branch as a function of wavenumber for $\tilde{c}_{\rm s} = 1/2$ and $\theta = \pi/4$. The horizontal line represents the sound speed. The black circles correspond to the six models used in the convergence test conducted in Section 3.4.

2.2. Review of Properties of Linear Waves in Hall-MHD

Although linear Hall-MHD wave propagation tests are widely used to evaluate various methods, most studies focus primarily on incompressible waves propagating along the unperturbed magnetic field. Thus, it remains unclear whether these methods can accurately capture other types of linear waves. In this study, we assess the performance of various methods on all linear waves in Section 3.4. This section provides a brief review of the physical properties of the linear waves in Hall-MHD (e.g., E. Hameiri et al. 2005).

We consider a uniform static gas with a density of ρ_0 and a uniform magnetic field of $\boldsymbol{B}_0$ as the unperturbed state. The sound speed and Alfvén speed in the unperturbed state are denoted by $c_{\rm s}$ and $c_{\rm A}$, respectively. We analyze perturbations proportional to $e^{i(\boldsymbol{k}\cdot\boldsymbol{x} - \omega t)}$, where $\boldsymbol{k}$ is the wavenumber vector and ω is the angular frequency. Linearizing Equations (1)–(4) with $\eta_{\rm O} = \eta_{\rm A} = 0$ yields the following dispersion relation:

$$\left(\frac{\omega}{c_{\rm A}k}\right)^6 - \{\tilde{c}_{\rm s}^2 + 1 + \cos^2\theta + (kL_{\rm H})^2\cos^2\theta\}\left(\frac{\omega}{c_{\rm A}k}\right)^4 + \{\tilde{c}_{\rm s}^2(kL_{\rm H})^2\cos^2\theta + (2\tilde{c}_{\rm s}^2 + 1)\cos^2\theta\}\left(\frac{\omega}{c_{\rm A}k}\right)^2 - \tilde{c}_{\rm s}^2\cos^4\theta = 0, \tag{7}$$

where $\tilde{c}_{\rm s} = c_{\rm s}/c_{\rm A}$, $k = |\boldsymbol{k}|$, and θ is the angle between $\boldsymbol{k}$ and $\boldsymbol{B}_0$. The Hall scale, $L_{\rm H}$, is defined as

$$L_{\rm H} = \frac{\eta_{\rm H}}{c_{\rm A}} \tag{8}$$

(B. P. Pandey & M. Wardle 2008). For a fully ionized plasma, $L_{\rm H}$ corresponds to the ion skin depth. When $kL_{\rm H} > 1$, the dispersion relation deviates from that of ideal MHD due to the Hall effect.

Figure 1 shows the dispersion relation for $\tilde{c}_{\rm s} = 1/2$ and $\theta = \pi/4$. As in ideal MHD, three branches appear. In ascending

order of phase speeds, they are referred to as the "slow-wave branch," the "Alfvén-wave branch," and the "fast-wave branch." In the low-wavenumber limit, $kL_H \ll 1$, the slow-wave branch, Alfvén-wave branch, and fast-wave branch correspond to the slow, Alfvén, and fast waves, respectively.

For $kL_H \gg 1$, the phase speeds of the fast-wave and slow-wave branches are no longer constant with respect to the wavenumber, due to the Hall effect. The fast-wave branch corresponds to whistler waves, for which the phase speed is

$$\frac{\omega}{c_A k} \sim kL_H \cos\theta. \tag{9}$$

Whistler waves are right-hand circularly polarized. The magnetic field perturbations oscillate rapidly, while the gas remains nearly static. The velocity perturbations are negligible compared to the magnetic field perturbations divided by $\sqrt{4\pi\rho_0}$, where ρ_0 is the unperturbed density.

For $kL_H \gg 1$, the slow-wave branch asymptotically approaches the ion-cyclotron wave, for which the phase speed is given by

$$\frac{\omega}{c_A k} \sim (kL_H)^{-1} \cos\theta. \tag{10}$$

Ion-cyclotron waves, which are left-hand circularly polarized, cannot oscillate at frequencies higher than the ion-cyclotron frequency, which is given by c_A/L_H for $\theta = 0$. Unlike whistler waves, velocity perturbations dominate relative to magnetic field perturbations divided by $\sqrt{4\pi\rho_0}$.

As kL_H increases, the Alfvén-wave branch transitions from an Alfvén wave to a sound wave around $kL_H \sim 1$. Thus, in the Hall-dominated regime ($kL_H \gg 1$), the compressible mode (sound wave) decouples from the incompressible modes (whistler and ion-cyclotron waves).

For $\tilde{c}_s = 1/2$, a mode exchange occurs around $kL_H \sim 1$ between the Alfvén-wave and slow-wave branches. The Alfvén-wave (slow-wave) branch transitions from an incompressible (compressible) state to a compressible (incompressible) state. For gases with $\tilde{c}_s$ larger than unity, a similar mode exchange occurs between the fast-wave and Alfvén-wave branches.

2.3. Implementations of Hall Effect Considered in This Study

A simple implementation of the Hall effect involves adding the Hall electric field to the electric field used to update the magnetic field, without further modifications to the numerical scheme (see Section 2.4). As mentioned in Section 1, a third-order time integrator is conditionally stable against infinitesimally small perturbations, whereas first- and second-order time integrators are unstable (S. A. E. G. Falle 2003; M. W. Kunz & G. Lesur 2013). As demonstrated in Section 3.1, even with a third-order time integrator, nonlinear numerical instabilities arise near the Nyquist wavelength when perturbation amplitudes are large.

To suppress numerical instabilities, various implementations have been proposed in the literature. In this section, in addition to the simple implementation, we introduce three methods for comparison in this study. The implementation details of these methods in `Athena++` are described in Section 2.4.

2.3.1. HALL-HLL

Since the Hall effect modifies the phase speeds of linear waves (Section 3.4), it is natural to modify the Riemann solver used to compute the numerical fluxes. The Hall effect makes the phase speeds of waves wavenumber-dependent (Figure 1). It is challenging to construct a Riemann solver incorporating the Hall effect, because self-similarity no longer holds in the Riemann problem. Among various approximate Riemann solvers, the HLL method (A. Harten et al. 1983) can be applied to any problem by setting signal speeds appropriately. G. Lesur et al. (2014) modified the HLL numerical flux by incorporating the phase speed of whistler waves. This method is referred to as HALL-HLL.

In the HLL scheme (A. Harten et al. 1983), by considering two waves propagating at the signal speeds S_L and S_R from the initial discontinuity at the cell boundary, the numerical flux at the cell boundary is constructed as follows:

$$\boldsymbol{F}_{\rm HLL} = \begin{cases} \boldsymbol{F}_L & S_L > 0 \\ \boldsymbol{F}_R & S_R < 0 \\ \dfrac{S_R S_L (\boldsymbol{U}_R - \boldsymbol{U}_L) + S_R \boldsymbol{F}_L - S_L \boldsymbol{F}_R}{S_R - S_L} & \text{otherwise,} \end{cases} \tag{11}$$

where $\boldsymbol{U}_L$ and $\boldsymbol{U}_R$ are the conserved variables of the left and right states, and $\boldsymbol{F}_L$ and $\boldsymbol{F}_R$ are the corresponding fluxes. Expressions of the signal speeds S_L and S_R are replaced with

$$S_L = \min(v_L - c_{\rm max,L},\, v_R - c_{\rm max,R}) \tag{12}$$

and

$$S_R = \max(v_L + c_{\rm max,L},\, v_R + c_{\rm max,R}), \tag{13}$$

respectively (S. F. Davis 1988), where v_L and v_R are the normal velocities of the left and right states, respectively. $c_{\rm max,L}$ ($c_{\rm max,R}$) is the maximum phase speed $c_{\rm max}$ of the left (right) state. In ideal MHD, the phase speed of fast waves c_f is assigned to $c_{\rm max}$. Note that there are other options for the expressions of $S_{L,R}$ (e.g., B. Einfeldt 1988).

In HALL-HLL, $c_{\rm max}$ is given by

$$c_{\rm max} = \max(c_f,\, c_w(k_{\rm max})), \tag{14}$$

where c_w is the phase speed of whistler waves propagating along the magnetic field,

$$c_w(k) = \frac{\eta_H k}{2} + \sqrt{\left(\frac{\eta_H k}{2}\right)^2 + c_A^2}, \tag{15}$$

and $k_{\rm max}$ is the maximum wavenumber that can be resolved in numerical simulations.

Various values of $k_{\rm max}$ were used in previous studies. G. Lesur et al. (2014) and X.-N. Bai & J. M. Stone (2017) adopted $k_{\rm max} = \Delta x^{-1}$, while P. Marchand et al. (2018) employed a larger value of $k_{\rm max} = \pi\Delta x^{-1}$ that corresponds to the Nyquist wavenumber. In this study, $k_{\rm max} = \Delta x^{-1}$ is adopted, because the results of G. Lesur et al. (2014) and X.-N. Bai & J. M. Stone (2017) demonstrate that $k_{\rm max} = \Delta x^{-1}$ is sufficiently large to suppress numerical instabilities caused by the Hall effect.

The numerical dissipation introduced by HALL-HLL is estimated from the induction equation. For simplicity, we consider a one-dimensional problem where the Hall effect dominates ($c_w(\Delta x^{-1}) \gg c_f$) and the flow speed is significantly lower than $c_w(\Delta x^{-1})$. From Equations (12), (13), and (14), the signal speeds are given by $S_L = -c_w(\Delta x^{-1})$ and $S_R = c_w(\Delta x^{-1})$. G. Tóth et al. (2008) derived the following

Table 1
List of the Implementations Evaluated in This Paper

Method Name	Description of Implementation
HLLD	No modifications are made in Athena++ except for the addition of the Hall term to the electric field used to update the magnetic field in the CT method.
HALL-HLL	The HALL-HLL numerical flux is used instead of HLLD (Equation (11); G. Lesur et al. 2014).
HALL-HLLMOD	The HALL-HLL numerical flux is used to update the magnetic field (Equation (11)). For other variables, the numerical fluxes are calculated by replacing $c_{\max}$ with $c_{\rm f}$ (P. Marchand et al. 2019).
HYP-RESIS	A fourth-order hyper-resistivity is added into the electric field (Equation (17); J. Birn et al. 2001).

equation:

$$\left(\frac{\partial \boldsymbol{B}_\perp}{\partial t}\right)_{\rm HALL-HLL} \sim -\frac{c_{\rm w}(\Delta x^{-1})\Delta x^3}{8}\frac{\partial^4 \boldsymbol{B}_\perp}{\partial x^4} \sim -\frac{\eta_{\rm H}\Delta x^2}{8}\frac{\partial^4 \boldsymbol{B}_\perp}{\partial x^4}, \quad (16)$$

where Equation (15) is applied in the limit $\eta_{\rm H}\Delta x^{-1} \gg c_{\rm A}$.

2.3.2. Modified HALL-HLL

P. Marchand et al. (2018) found that the use of HALL-HLL significantly violates angular momentum conservation in simulations of gravitational collapse of dense cores in Cartesian coordinates.

A modified version of HALL-HLL was proposed by P. Marchand et al. (2019). This method is referred to as HALL-HLLMOD in this paper. In HALL-HLLMOD, Equation (14) is exclusively used to compute the numerical fluxes for the magnetic field. For other components of the numerical fluxes used to update the hydrodynamic variables (ρ, $\rho\boldsymbol{v}$, E), the original HLL numerical flux is applied. It has been found that HALL-HLLMOD significantly improves angular momentum conservation in collapsing dense cores.

2.3.3. Hyper-resistivity

Hyper-resistivity is introduced into the electric field as follows:

$$\boldsymbol{E}_{\rm hyp} = -\frac{4\pi}{c}\eta_{\rm hyp}\boldsymbol{\nabla}^2\boldsymbol{J}, \quad (17)$$

where $\eta_{\rm hyp}$ is a coefficient (J. Birn et al. 2001; Z. W. Ma & A. Bhattacharjee 2001). The coefficient $\eta_{\rm hyp}$ must be sufficiently large to suppress numerical instabilities but small enough to ensure accurate results.

To ensure that the time-step limitation imposed by hyper-resistivity is less restrictive than that imposed by the Hall effect for any Δx and $\eta_{\rm H}$, the coefficient is defined as follows:

$$\eta_{\rm hyp} = C_{\rm hyp}\eta_{\rm H}\Delta x^2, \quad (18)$$

where $C_{\rm hyp}$ is a free parameter. L. Chacón & D. A. Knoll (2003) employed a similar coefficient to develop a two-dimensional implicit Hall-MHD solver. A possible range of $C_{\rm hyp}$ is estimated in Section 3.2.2.

In a one-dimensional problem, the dissipation term due to the hyper-resistivity is expressed as

$$\left(\frac{\partial \boldsymbol{B}_\perp}{\partial t}\right)_{\rm HYP-RESIS} = -C_{\rm hyp}\eta_{\rm H}\Delta x^2\frac{\partial^4 \boldsymbol{B}_\perp}{\partial x^4} \quad (19)$$

in the long-wavelength limit. Comparison between Equations (16) and (19) shows that their dissipation terms are identical when $C_{\rm hyp} = 0.125$.

2.4. Implementations of Hall Effect in Athena++

We implement the four methods listed in Table 1 in Athena++ (J. M. Stone et al. 2020). For all methods, we use the third-order strong-stability-preserving Runge–Kutta time integrator that is referred to as RK3 (S. Gottlieb et al. 2009, Equation (3.1)) and the piecewise linear spatial reconstruction with the van Leer limiter (B. van Leer 1974). Except for HALL-HLL and HALL-HLLMOD, the HLLD numerical flux without modifying the signal speeds is used (T. Miyoshi & K. Kusano 2005).

Athena++ employs a staggered grid for the CT scheme. The conserved hydrodynamical variables (ρ, $\rho\boldsymbol{v}$, E) are averaged within the cell volume and defined at the cell volume center. The normal components of the magnetic field $\boldsymbol{B}$ are averaged on cell surfaces and are defined at the cell surface center. In this paper, we consider only Cartesian coordinates.

The cell center coordinates are denoted by (x_i, y_j, z_k), where i, j, k represent the discrete cell indices. A cell-centered variable, U, at (x_i, y_j, z_k) is expressed as $U_{i,j,k}$. The positions of the cell surfaces between the (i, j, k)th and $(i+1, j, k)$th cells are denoted as $(x_{i+1/2}, y_j, z_k)$. The x-component of the magnetic field defined at $(x_{i+1/2}, y_j, z_k)$ is $(B_x)_{i+1/2,j,k}$. Similarly, the y- and z-components of the magnetic field are denoted as $(B_y)_{i,j+1/2,k}$ and $(B_z)_{i,j,k+1/2}$, respectively.

The hydrodynamical variables (ρ, $\rho\boldsymbol{v}$, E) are updated by computing the numerical fluxes using a Riemann solver. In deriving the numerical fluxes, the cell-centered magnetic fields are computed as follows:

$$\begin{aligned}(B_x)_{i,j,k} &= \frac{1}{2}\{(B_x)_{i-\frac{1}{2},j,k} + (B_x)_{i+\frac{1}{2},j,k}\}\\ (B_y)_{i,j,k} &= \frac{1}{2}\{(B_y)_{i,j-\frac{1}{2},k} + (B_y)_{i,j+\frac{1}{2},k}\}\\ (B_z)_{i,j,k} &= \frac{1}{2}\{(B_z)_{i,j,k-\frac{1}{2}} + (B_z)_{i,j,k+\frac{1}{2}}\}.\end{aligned} \quad (20)$$

To update the surface-centered components of the magnetic field, the electric field components at the cell edges are computed —namely, $(E_x)_{i,j+1/2,k+1/2}$, $(E_y)_{i+1/2,j,k+1/2}$, $(E_z)_{i+1/2,j+1/2,k}$. The electric fields from ideal MHD ($-\boldsymbol{v}\times\boldsymbol{B}$) are calculated using the method proposed by T. A. Gardiner & J. M. Stone (2005, 2008).

2.4.1. Inclusion of the Hall Term in the Induction Equation

Similar to ohmic diffusion and ambipolar diffusion, the Hall effect is incorporated into the cell-edge electric fields. Discretized expressions of the electric currents, defined at the

cell edges, are given by

$$(J_x)_{i,j+\frac{1}{2},k+\frac{1}{2}} = \frac{(B_z)_{i,j+1,k+\frac{1}{2}} - (B_z)_{i,j,k+\frac{1}{2}}}{\Delta y} - \frac{(B_y)_{i,j+\frac{1}{2},k+1} - (B_y)_{i,j+\frac{1}{2},k}}{\Delta z}. \quad (21)$$

The remaining components, $(J_y)_{i+1/2,j,k+1/2}$ and $(J_z)_{i+1/2,j+1/2,k}$, are computed in the same manner.

The x-component of the electric field induced by the Hall effect is given by

$$(E_x)_{i,j+\frac{1}{2},k+\frac{1}{2}} = \frac{(\eta_{\rm H})_{i,j+\frac{1}{2},k+\frac{1}{2}}}{|\boldsymbol{B}_{i,j+\frac{1}{2},k+\frac{1}{2}}|} \times [(J_y)_{i,j+\frac{1}{2},k+\frac{1}{2}}(B_z)_{i,j+\frac{1}{2},k+\frac{1}{2}} - (J_z)_{i,j+\frac{1}{2},k+\frac{1}{2}}(B_y)_{i,j+\frac{1}{2},k+\frac{1}{2}}]. \quad (22)$$

The quantities in Equation (22) defined at the cell edge $(x_i, y_{j+1/2}, z_{k+1/2})$ are calculated as follows:

$$(\eta_{\rm H})_{i,j+\frac{1}{2},k+\frac{1}{2}} = \frac{1}{4}\sum_{kl=0}^{1}\sum_{jl=0}^{1}(\eta_{\rm H})_{i,j+jl,k+kl},$$

$$(B_x)_{i,j+\frac{1}{2},k+\frac{1}{2}} = \frac{1}{8}\sum_{il=0}^{1}\sum_{jl=0}^{1}\sum_{kl=0}^{1}(B_x)_{i-\frac{1}{2}+il,j+il,k+kl},$$

$$(B_y)_{i,j+\frac{1}{2},k+\frac{1}{2}} = \frac{1}{2}\{(B_y)_{i,j-\frac{1}{2},k} + (B_y)_{i,j+\frac{1}{2},k}\},$$

$$(B_z)_{i,j+\frac{1}{2},k+\frac{1}{2}} = \frac{1}{2}\{(B_z)_{i,j,k-\frac{1}{2}} + (B_z)_{i,j,k+\frac{1}{2}}\},$$

$$(J_y)_{i,j+\frac{1}{2},k+\frac{1}{2}} = \frac{1}{4}\sum_{il=0}^{1}\sum_{jl=0}^{1}(J_y)_{i-\frac{1}{2}+il,j+jl,k+\frac{1}{2}},$$

and

$$(J_z)_{i,j+\frac{1}{2},k+\frac{1}{2}} = \frac{1}{4}\sum_{il=0}^{1}\sum_{kl=0}^{1}(J_z)_{i-\frac{1}{2}+il,j+\frac{1}{2},k+kl}.$$

2.4.2. Implementations of Hyper-resistivity

The hyper-resistivity coefficient $\eta_{\rm hyp}$ shown in Equation (18) can be applied only when $\Delta x = \Delta y = \Delta z$. To satisfy the stability condition, Δx^2 in Equation (18) is replaced with $\min(\Delta x^2, \Delta y^2, \Delta z^2)$. The discretized form of hyper-resistivity is given as follows:

$$(E_{x,\rm hyp})_{i,j+\frac{1}{2},k+\frac{1}{2}} = C_{\rm hyp}(\eta_{\rm H})_{i,j+\frac{1}{2},k+\frac{1}{2}} \times \min(\Delta x^2, \Delta y^2, \Delta z^2) \times \Delta_{\rm L}(J_x)_{i,j+\frac{1}{2},k+\frac{1}{2}}, \quad (23)$$

where $\Delta_{\rm L}$ represents the discrete Laplacian operator, defined as

$$\Delta_{\rm L}Q_{i,j,k} = \frac{1}{\Delta x^2}(Q_{i-1,j,k} - 2Q_{i,j,k} + Q_{i+1,j,k}) + \frac{1}{\Delta y^2}(Q_{i,j-1,k} - 2Q_{i,j,k} + Q_{i,j+1,k}) + \frac{1}{\Delta z^2}(Q_{i,j,k-1} - 2Q_{i,j,k} + Q_{i,j,k+1}), \quad (24)$$

assuming a uniform grid spacing.

2.4.3. Time-step Constraint due to the Hall Effect

Based on the von Neumann stability analysis (see the Appendix), the time-step constraint imposed by the Hall effect is expressed as

$$\Delta t_{\rm H} = \frac{C_{\rm H}}{4}\sqrt{\frac{3}{d}}\min_{i,j,k}\left\{\frac{\min(\Delta x^2, \Delta y^2, \Delta z^2)}{(\eta_{\rm H})_{i,j,k}}\right\}, \quad (25)$$

where d represents the spatial dimension. In this study, $C_{\rm H}$ is set to 0.8.

3. Numerical Experiments

3.1. Stability of Hall-MHD with HLLD

M. W. Kunz & G. Lesur (2013) demonstrated that Hall-MHD with third-order time integrators is conditionally stable in the absence of dissipation, whereas second-order time integrators lead to numerical instability for any Δt (see also S. A. E. G. Falle 2003). In this section, we analyze the stability of the RK3 integrator through whistler wave propagation tests.

In the whistler wave propagation test, most studies focus on waves propagating exclusively along the unperturbed magnetic field. To explore a more general situation, we examine a whistler wave propagating at an angle relative to the wavenumber vector $\boldsymbol{k}$.

The wavenumber vector is inclined relative to the grid (T. A. Gardiner & J. M. Stone 2008; A. Mignone et al. 2010). The wavenumber vector $\boldsymbol{k}$ is set to 2π (1, 2, 2)/3. The unit vector along the x-axis is converted into $\boldsymbol{k}/|\boldsymbol{k}|$ using the rotation matrix:

$$\mathcal{R} = \begin{pmatrix}\cos\theta_1 & -\sin\theta_1 & 0\\ \sin\theta_1 & \cos\theta_1 & 0\\ 0 & 0 & 1\end{pmatrix}\cdot\begin{pmatrix}\cos\theta_2 & 0 & -\sin\theta_2\\ 0 & 1 & \\ \sin\theta_2 & 0 & \cos\theta_2\end{pmatrix}, \quad (26)$$

where $\tan\theta_1 = 2$ and $\tan\theta_2 = 2/\sqrt{5}$.

The coordinates $\boldsymbol{\xi} = (\xi, \eta, \zeta)$ are defined as $\mathcal{R}\boldsymbol{x}$, aligning the wavenumber vector $\boldsymbol{k}$ to the ξ-axis. The unperturbed magnetic field $\boldsymbol{B}_0$ is tilted by $\theta_{\rm B}$ with respect to the ξ-axis in the (ξ, η) plane, where $\boldsymbol{B}_0 = (B_{\xi 0}\cos\theta_{\rm B}, B_{\eta 0}\sin\theta_{\rm B}, 0)$.

The Hall coefficient $\eta_{\rm H}$ is set so that $kL_{\rm H} = 2\times 10^4\pi$. For $kL_{\rm H} \gg 1$, the gas remains static in the fast-wave branch, which corresponds to whistler waves. Thus, perturbations are introduced exclusively in the magnetic field as follows:

$$\delta B_\xi = 0, \quad \delta B_\eta = A\sin(k\xi), \quad \delta B_\zeta = A\cos(k\xi), \quad (27)$$

where A represents the initial amplitude and $k = |\boldsymbol{k}|$. The dispersion relation of the whistler waves is

$$\frac{\omega}{k} = \frac{\eta_{\rm H}k\cos\theta_{\rm B}}{2} + \sqrt{\left(\frac{\eta_{\rm H}k\cos\theta_{\rm B}}{2}\right)^2 + c_{\rm A}^2\cos^2\theta_{\rm B}}. \quad (28)$$

The computational box spans $0 \leqslant x \leqslant 2$ and $0 \leqslant y, z \leqslant 1$, and is discretized into $N \times (N/2) \times (N/2)$ cells. Periodic boundary conditions are imposed in all directions. Numerical instabilities caused by the Hall effect are expected to develop around the Nyquist wavelength. A small value of $N = 16$ is used to promote numerical instabilities.

We consider two values for the initial amplitude ($A = 10^{-3}$ and 10^{-1}) and analyze how the propagation of the whistler waves depends on A and $\theta_{\rm B}$.

Figure 2(a) presents the results for the smaller amplitude, $A = 10^{-3}$. For all $\theta_{\rm B}$, the time evolution of $\delta B = (\langle\delta B_x^2\rangle + \langle\delta B_y^2\rangle + \langle\delta B_z^2\rangle)^{1/2}$ is consistent with the predictions

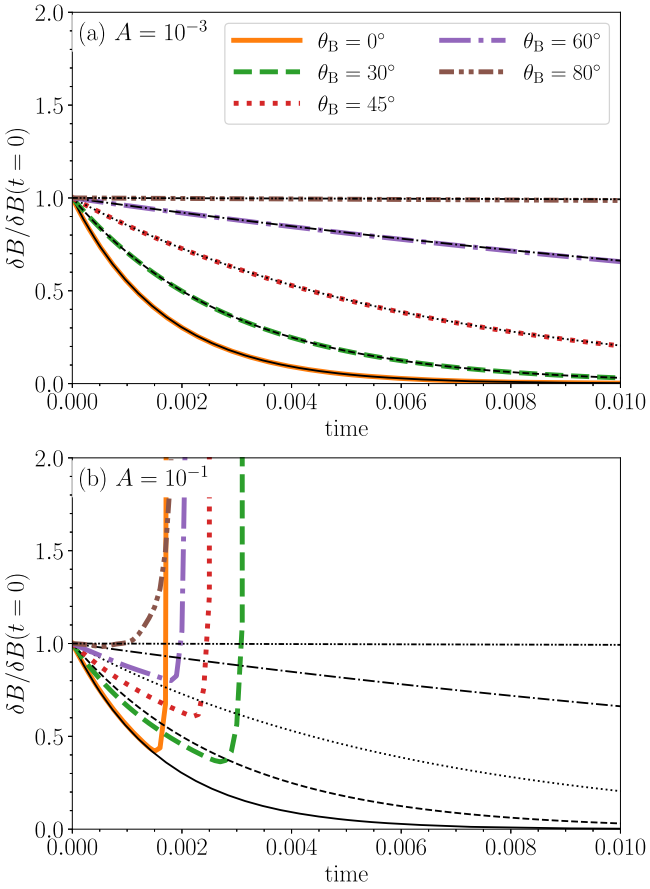

Figure 2. Time evolution of $\delta B = (\langle \delta B_x^2 \rangle + \langle \delta B_y^2 \rangle + \langle \delta B_z^2 \rangle)^{1/2}$ for (a) $A = 10^{-3}$ and (b) $A = 10^{-1}$. The results with five different θ_B (0°, 30°, 45°, 60°, and 80°) are shown. The thin lines represent the predictions from the von Neumann stability analysis presented in the Appendix. The differences in the line style indicate variations in θ_B.

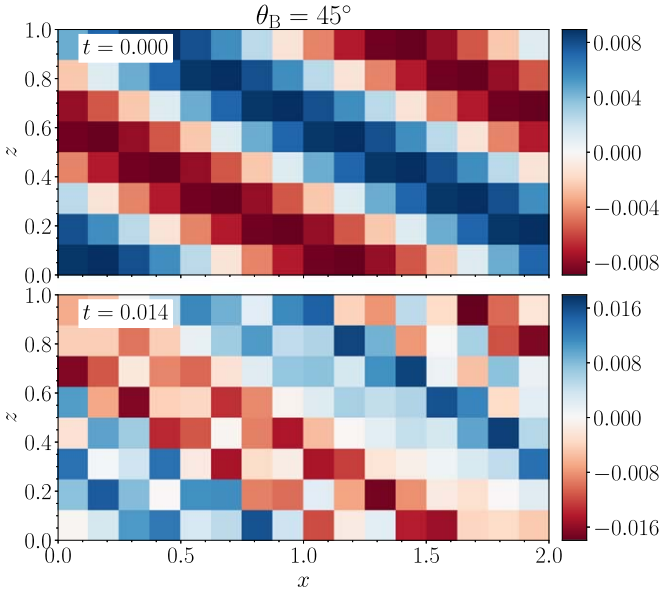

Figure 3. Two-dimensional slice of δB_z at $y = 0.5$. The top panel shows the initial condition, and the bottom panel shows the δB_z map when the amplitude of δB_z has increased by a factor of 2.

from the von Neumann stability analysis presented in the Appendix. Minor discrepancies between the numerical results and theoretical predictions are attributed to numerical dissipation introduced by the HLLD solver that is not considered in the von Neumann stability analysis.

When A increases from 10^{-3} to 10^{-1}, its behavior changes significantly. Numerical instabilities occur suddenly and δB increases rapidly at the grid scale for all the cases. Figure 3 compares the B_z maps at $t = 0$ and shortly after the onset of the numerical instability. Grid-scale fluctuations in the magnetic field increase.

3.2. Turbulent Magnetic Field

In this test problem, we first measure the growth rate of the numerical instability induced by the Hall effect in Section 3.2.1. Using both the growth rate and the results of the von Neumann stability analysis of Hall-MHD with hyper-resistivity (Appendix), we determine an appropriate range of $C_{\rm hyp}$ in Section 3.2.2. The implementations listed in Table 1 are compared in Section 3.2.3.

Numerical instabilities caused by the Hall effect typically occur around the Nyquist wavelength. To evaluate the performance of the methods listed in Table 1, we initialize a uniform static gas ($\rho = 1$, $P = 1/\gamma$, $\boldsymbol{v} = 0$) with turbulent magnetic fields that exhibit white noise, where $\gamma = 5/3$. No net magnetic field is present.

To ensure that $\boldsymbol{\nabla} \cdot \boldsymbol{B} = 0$ within roundoff errors, the initial magnetic field is derived from a turbulent vector potential field, with a power spectrum designed to generate white noise in the face-centered magnetic field fluctuation. The initial amplitude of the magnetic field perturbation is defined as $\sqrt{\langle \delta \boldsymbol{B}^2 \rangle} = \sqrt{4\pi}$, where $\langle Q \rangle$ denotes the volume average of Q. Note that the results do not depend on the field strength, because the induction equation, which considers only the Hall electric field, is linear with respect to $\boldsymbol{B}$ when η_H is constant, as long as the phase speed of the whistler wave at the grid scale is significantly larger than the Alfvén speed and sound speed.

In addition, as shown in Section 2.2, in whistler waves, magnetic field perturbations dominate over other perturbations. In other words, the gas is almost static during the development of the magnetic field.

The computational domain spans $0 \leqslant x, y, z \leqslant L$ and is discretized into 32^3 cells, with periodic boundary conditions applied in all directions.

3.2.1. Measuring a Growth Rate of the Numerical Instabilities due to the Hall Effect

Before presenting the results of the four implementations, we estimate the growth rate of the numerical instabilities caused by the Hall effect. In this test, HLLD is used.

Since the numerical instabilities primarily develop around the Nyquist wavelength, the characteristic timescale is expected to correspond to the crossing time of the whistler wave across this wavelength:

$$t_w = \frac{2\Delta x^2}{\pi \eta_H}, \tag{29}$$

where we use the phase speed of the whistler wave at the Nyquist wavelength $\eta_H \pi / \Delta x$. Thus, the growth rate σ can be

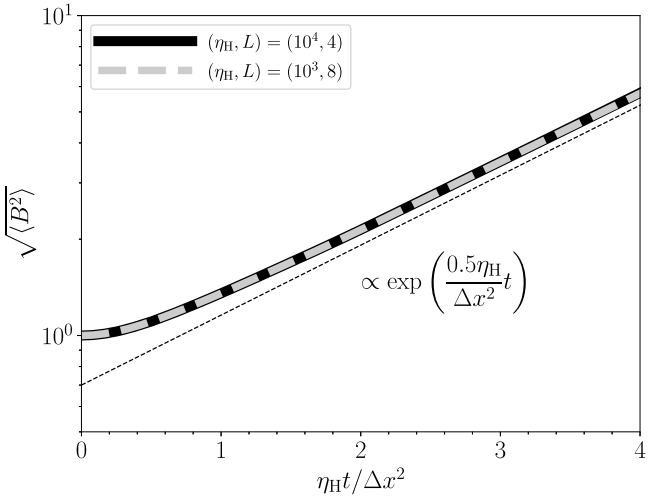

Figure 4. Time evolution of $\sqrt{\langle \delta B^2 \rangle}$ for the two parameter sets ($\eta_{\rm H} = 10^4$, $L = 4$) and ($\eta_{\rm H} = 10^3$, $L = 8$). The thin dashed line represents the estimated growth rate.

parameterized as

$$\sigma_{\rm inst} = C_\sigma \frac{\eta_{\rm H}}{\Delta x^2}, \tag{30}$$

where C_σ is a parameter that is determined by the numerical experiment shown below.

Figure 4 shows the time evolution of $\sqrt{\langle \delta B^2 \rangle}$ for the two parameter sets, ($\eta_{\rm H} = 10^4$, $L = 4$) and ($\eta_{\rm H} = 10^3$, $L = 8$). The two lines are almost identical when the normalized time $\eta_{\rm H}t/\Delta x^2$ is taken as the horizontal axis. This clearly shows that the growth rate $\sigma_{\rm inst}$ is proportional to $t_{\rm w}^{-1} \sim \eta_{\rm H}\Delta x^{-2}$. Fitting the results with $\exp(\sigma_{\rm inst}t)$ yields $C_\sigma = 0.5$.

3.2.2. Appropriate Range of the Hyper-resistivity Coefficient

The minimum value of $C_{\rm hyp}$ is determined by the condition that the damping rate caused by the hyper-resistivity exceeds the growth rate σ of the numerical instability.

By linearizing the discretized induction equation solved in `Athena++`, we obtain a damping rate of $C_{\rm hyp}\eta_{\rm H}16d_{\rm Ny}^2\Delta x^{-2}$, considering only the hyper-resistivity in the linear analysis, assuming cubic cells ($\Delta x = \Delta y = \Delta z$), where $d_{\rm Ny}$ denotes the number of directions containing Nyquist wavelength fluctuations. Therefore, $C_{\rm hyp}$ must meet the condition

$$C_{\rm hyp} > C_{\rm hyp,min} \sim 0.03 d_{\rm Ny}^{-2}. \tag{31}$$

Note that since $d_{\rm Ny} = 1$ is adopted to obtain a stricter condition for $C_{\rm hyp}$, $C_{\rm hyp,min} \sim 0.03$ should be regarded as an upper limit of $C_{\rm hyp,min}$.

The maximum value of $C_{\rm hyp}$ is determined by the condition that the time-step constraint caused by hyper-resistivity, $\Delta t_{\rm hyp}$, is greater than $\Delta t_{\rm H}$. From the von Neumann stability analysis, $\Delta t_{\rm hyp} \propto d^2\Delta x^2/\eta_{\rm H}$ can be obtained. By conducting numerical experiments on the turbulent magnetic field with different $C_{\rm H}$, d, and $C_{\rm hyp}$, we found that $C_{\rm hyp}$ must satisfy the following condition,

$$C_{\rm hyp} < C_{\rm hyp,max} = 0.09\left(\frac{d}{3}\right)^{-3/2}\left(\frac{C_{\rm H}}{0.8}\right)^{-1}, \tag{32}$$

in order for $\Delta t_{\rm hyp}$ not to affect the CFL condition (Section 2.4.3).

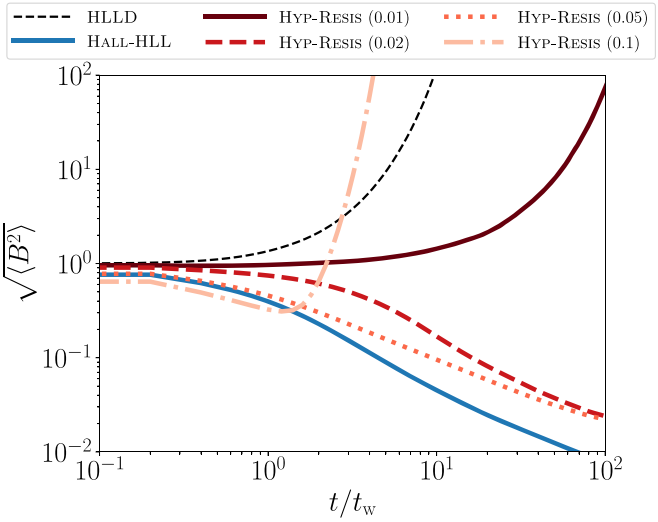

Figure 5. Time evolution of the magnetic field fluctuations. The results obtained using various methods (HLLD, Hall-HLL, and Hyp-Resis with $C_{\rm hyp} = 0.01$, 0.02, 0.05, and 0.1) are shown.

3.2.3. Comparison Between Different Implementations

We compare the results from the four implementations listed in Table 1. Here, we set $\eta_{\rm H} = 10^4$ and $L = 4$. The results for Hall-HLLmod are omitted in this section, as they are nearly identical to those of Hall-HLL, because the gas remains nearly static in this test.

A comparison of the results obtained using HLLD, Hall-HLL, and Hyp-Resis is shown in Figure 5. For Hyp-Resis, the runs with $0.01 < C_{\rm hyp} < 0.1$ produce stable results, whereas those with $C_{\rm hyp} = 0.01$ and 0.1 show numerical instabilities. This is roughly consistent with the requirement that $C_{\rm hyp}$ should be greater than $C_{\rm hyp,min} \sim 0.03$ and less than $C_{\rm hyp,max}$ (Section 3.2.2). Hall-HLL is also stable, but it reduces $\langle \sqrt{\delta \boldsymbol{B}^2} \rangle$ faster than Hyp-Resis.

In order to examine the magnetic field structure of the stable results, we present the B_x slice map at $z = L/2$ in Figure 6. First, the results with Hyp-Resis are analyzed. Grid-scale fluctuations, which persist for $C_{\rm hyp} = 0.02$, disappear in the B_x maps for $C_{\rm hyp} = 0.05$.

Hall-HLL exhibits significantly distinct features compared to Hyp-Resis, as shown in Figure 6. At $t = 10t_{\rm w}$, grid-scale disturbances remain in Hall-HLL, whereas large-scale fluctuations are less pronounced in Hall-HLL compared to Hyp-Resis with $C_{\rm hyp} = 0.05$. This is due to the fact that Hall-HLL utilizes the cell-centered transverse magnetic fields rather than the face-centered magnetic fields when computing the numerical fluxes (Section 2.4). Since cell-centered magnetic fields are derived by using a simple arithmetic average of face-centered magnetic fields (Equation (20)), grid-scale disturbances of the face-centered magnetic fields are significantly reduced during the conversion from the face-centered $\boldsymbol{B}$ to the cell-centered $\boldsymbol{B}$. By contrast, the face-centered magnetic fields are used to compute the edge-centered electric field due to the hyper-resistivity. Thus, Hall-HLL is less effective in reducing pre-existing grid-scale perturbations in $\boldsymbol{B}$ than Hyp-Resis, which directly utilizes the face-centered $\boldsymbol{B}$.

3.3. Density-shear Instability

In this section, we investigate the density-shear instability as a numerical experiment involving variable $\eta_{\rm H}$. This instability

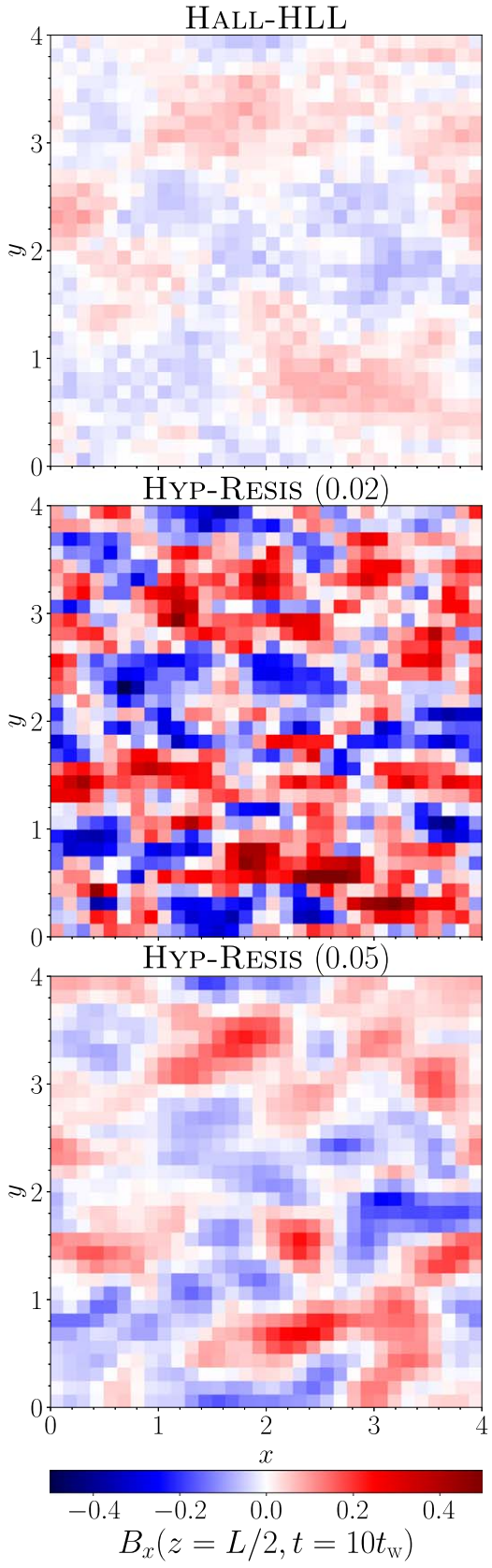

Figure 6. The B_x slice at $z = 2$ for Hall-HLL and Hyp-Resis ($C_{hyp} = 0.02$ and 0.05). The maps are taken at $t = 10t_w$.

occurs in situations where both the unperturbed magnetic field $\boldsymbol{B}_0$ and the electron number density have steep gradients perpendicular to $\boldsymbol{B}_0$ (T. S. Wood et al. 2014). The Hall effect coefficient η_H is given by $\eta_H = cB/(4\pi e n_e)$, where c is the speed of light, B is the magnetic field strength, e is the elementary electric charge, and n_e is the electron number density.

K. N. Gourgouliatos et al. (2015) conducted numerical simulations of the density-shear instability. We solve the full set of Hall-MHD equations (Equations (1)–(4)), whereas they considered the induction equation taking into account only the Hall electric field using a pseudo-spectral code. However, the results are expected to be consistent with those of K. N. Gourgouliatos et al. (2015), because the gas remains nearly static as the magnetic field evolves, similar to the turbulent magnetic field test (Section 3.2).

Following K. N. Gourgouliatos et al. (2015), we assume an unperturbed plane-parallel magnetic field, localized around $y = 0$ with a characteristic length scale of a, as follows:

$$B_x = B_0\left\{\exp\left(-\frac{y^2}{a^2}\right) + \epsilon_B\right\},\ B_y = B_z = 0, \tag{33}$$

where $\epsilon_B = 10^{-2}$ represents the magnetic field floor. The electron number density has a similar functional form to B_x:

$$n_e = n_0\left\{\exp\left(-\frac{y^2}{a^2}\right) + \epsilon_n\right\}, \tag{34}$$

where $\epsilon_n = 10^{-2}$ is a floor bound for n_e. We consider a fully ionized gas in which the density is proportional to n_e and is $\rho_0 = 1$ at $y = 0$. The initial gas pressure is set so that the total pressure $P + B_x^2/8\pi$ is spatially constant. The results are insensitive to the total pressure, because the gas remains nearly static throughout the evolution. In this study, we set $8\pi P/B_x^2 = 0.1$ for $y = 0$ and $B_0 = 1$.

From Equation (34), the Hall effect coefficient is expressed as

$$\eta_H = \eta_{H0}\frac{|\boldsymbol{B}|/B_0}{\rho/\rho_0}, \tag{35}$$

where $\eta_{H0} = cB_0/(4\pi e n_0)$ is the reference Hall effect coefficient and is assigned a value of 100.

T. S. Wood et al. (2014) demonstrated through linear analysis that the growth rate reaches its maximum when the perturbation wavenumber vector is aligned to the x-axis. The dispersion relation is given by

$$\sigma(k) = \frac{\eta_{H0}}{a^2}\sqrt{(ka)^2\{2 - (ka)^2\}}, \tag{36}$$

where σ represents the growth rate and k denotes the wavenumber along the x-axis (T. S. Wood et al. 2014). The maximum growth rate $\sigma_{max} = \eta_{H0}/a^2$ is obtained at $k = a^{-1}$.

The fastest-growing mode is applied to B_y as follows:

$$B_y = \delta B \cos(x/a), \tag{37}$$

where $\delta B = 10^{-4}B_0$ is the initial amplitude. No perturbations are introduced for the other variables.

The simulations are performed in two dimensions. The box size in the (x, y) plane spans $-3\pi a \leqslant x,\ y \leqslant 3\pi a$ and is discretized by 128^2 cells, where the characteristic scale is $a = 0.1$. The width a is resolved by $\sim$14 cells. We evaluate the four different implementations: HLLD, Hall-HLL, Hall-HLLMOD, and Hyp-Resis. To investigate an appropriate value of C_{hyp}, we test $C_{hyp} = 0.01$, 0.02, 0.05, 0.1.

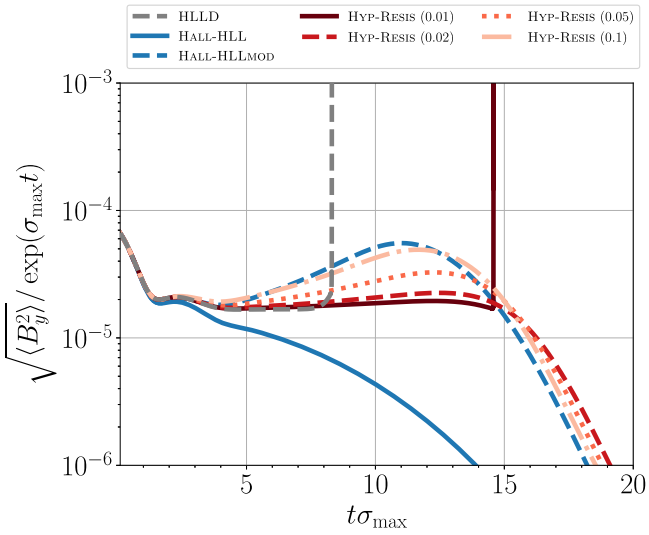

Figure 7. Time evolution of $\sqrt{\langle B_y^2\rangle}$ divided by $\exp(\sigma_{\max}t)$ for the four different implementations (HLLD, Hall-HLL, Hall-HLLmod, and Hyp-Resis with $C_{\rm hyp} = 0.01$, 0.02, 0.05, and 0.1). The horizontal axis is normalized by $\sigma_{\max}^{-1}$.

3.3.1. Linear Growth

First, the early-time evolution of $\langle B_y^2\rangle^{1/2}$ is compared to the theoretical predictions from the linear analysis in Figure 7. For HLLD, the evolution of $\langle B_y^2\rangle^{1/2}$ agrees with the expected trend $\exp(\sigma_{\max}t)$ until $t\sigma_{\max} \sim 8$, after which the numerical instability rapidly increases.

For Hall-HLL, $\langle B_y^2\rangle^{1/2}$ increases significantly slower than $\exp(\sigma_{\max}t)$, due to the large dissipation introduced in both the velocity and magnetic fields. The initially concentrated distributions of ρ and B_x along the y-axis (Equations (33) and (34)) become significantly diffused.

Next, we analyze the Hyp-Resis runs. When $C_{\rm hyp} = 0.01$, the growth rate agrees with $\sigma_{\max}$, but as $C_{\rm hyp}$ increases from 0.01, the growth rate departs from $\sigma_{\max}$. Counterintuitively, increasing $C_{\rm hyp}$ leads to an increased growth rate. This occurs because artificial diffusion is introduced exclusively in the magnetic field. As a result, the profiles of B_x undergo diffusion, while those of ρ remain nearly unchanged. This can be interpreted as setting a nonperturbed state where the width of the B_x profile (a_B) is slightly greater than that of the ρ profile (a_ρ). The growth rate increases with a_B at a fixed a_ρ (K. N. Gourgouliatos et al. 2015).

Hyp-Resis with lower $C_{\rm hyp}$ may experience numerical instabilities. Figure 7 indicates that the numerical instability arises for Hyp-Resis with $C_{\rm hyp} = 0.01$ around $t \sim 14.5$. The Hyp-Resis runs with $C_{\rm hyp} > 0.01$ appear to provide numerically stable results.

Hall-HLLmod produces more accurate results than Hall-HLL. The time evolution of $\langle B_y^2\rangle^{1/2}$ is close to that of Hyp-Resis with $C_{\rm hyp} = 0.1$. This occurs because the density profile diffusion is suppressed in Hall-HLLmod.

3.3.2. Nonlinear Evolution

Next, we investigate the nonlinear evolution of the density-shear instability. The snapshots at $t = 25$ are displayed in Figure 8. Corrugations in the magnetic field around $y = 0$ develop over time. When magnetic fields deform sufficiently, magnetic reconnection is triggered around pinched magnetic fields.

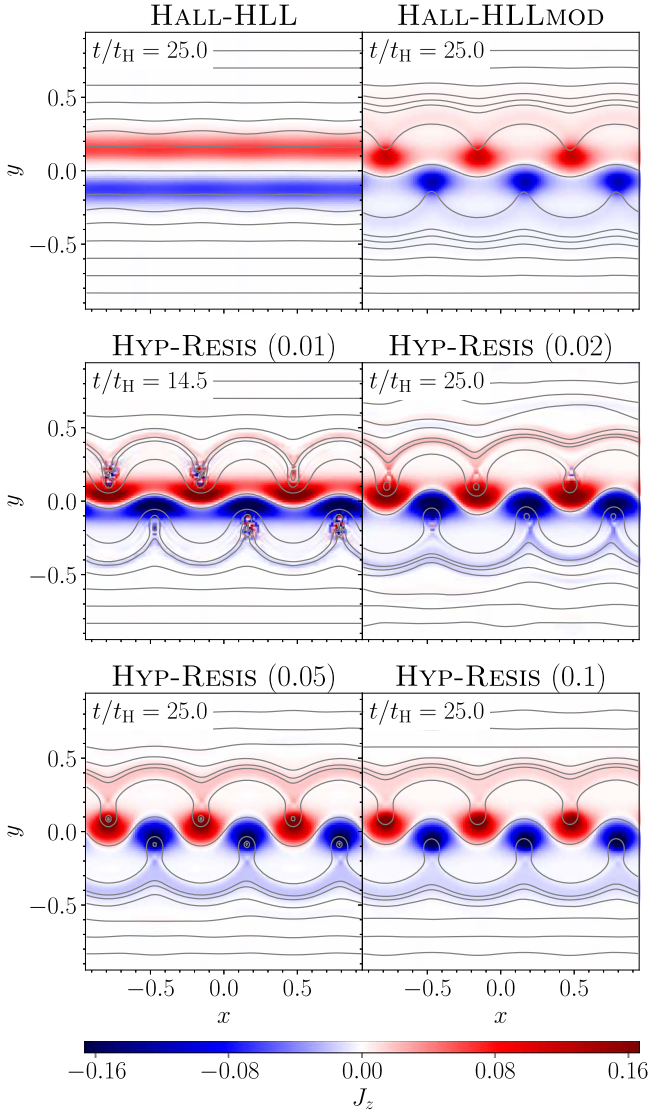

Figure 8. Color maps of the current density along the z-axis, J_z, for four different implementations (HLLD, Hall-HLL, Hall-HLLmod, and Hyp-Resis with $C_{\rm hyp} = 0.01$, 0.02, 0.05, and 0.1). The gray lines indicate the field lines in the x–y plane. The snapshots are taken at $t/t_{\rm H} = 25$. For Hyp-Resis with $C_{\rm hyp} = 0.01$, the J_z map is shown at the time when the numerical instability occurs.

As discussed in Section 3.3.1, the numerical instability arises at $t = 14.5$ in the Hyp-Resis case with $C_{\rm hyp} = 0.01$, particularly in the reconnection regions where J_z exhibits significant fluctuations. In the J_z map of Hyp-Resis with $C_{\rm hyp} = 0.02$, numerical wiggles are also seen around $(x, y) \sim (0.5, 0.2)$ and $(-0.5, -0.2)$. This indicates that $C_{\rm hyp} = 0.02$ leads to numerical fluctuations, due to insufficient dissipation. This is consistent with the fact that $C_{\rm hyp} = 0.02$ is less than $C_{\rm hyp,min} \sim 0.03$ (Equation (31)). No numerical oscillations are visible in the map of Hyp-Resis with $C_{\rm hyp} \geqslant 0.05$.

Compared to Hyp-Resis, Hall-HLL produces significantly more diffused results. The field lines are almost straight, indicating that the density-shear instability is almost suppressed. While Hall-HLLmod significantly improves the dissipative distribution of J_z, Figure 8 reveals that J_z in Hall-HLLmod remains more diffusive than Hyp-Resis with $C_{\rm hyp} = 0.1$.

3.4. Linear Wave Convergence Test

In Section 2.2, the physical properties of the fast-wave branch, Alfvén-wave branch, and slow-wave branch are discussed. In this section, we conduct convergence tests of linear waves in both uniform and static mesh refinement (SMR) grids.

The setup is as follows: we consider the propagation of linear waves at an inclination relative to the grid cells. The numerical setup follows that of Section 3.1, except that all types of linear waves are considered in this section. In the coordinate system $\boldsymbol{\xi} = (\xi, \eta, \zeta)$, defined as $\mathcal{R} \cdot \boldsymbol{x}$, the perturbation vector is defined as

$$\delta \boldsymbol{Q} = \left(c_{\rm s} \frac{\delta \rho}{\rho_0}, \delta v_\xi, \delta v_\eta, \delta v_\zeta, \frac{\delta B_\xi}{\sqrt{4\pi\rho_0}}, \frac{\delta B_\eta}{\sqrt{4\pi\rho_0}}, \frac{\delta B_\zeta}{\sqrt{4\pi\rho_0}} \right) \quad (38)$$

and has a spatial dependence of $e^{i\boldsymbol{k}\cdot\boldsymbol{\xi}}$. The initial perturbation amplitude is set to $|\delta \boldsymbol{Q}| = 10^{-6} c_{\rm A}$.

The simulation box spans $0 \leqslant x \leqslant L$, $0 \leqslant y, z \leqslant L/2$ and is divided by $N \times (N/2) \times (N/2)$ cells, where $L = 6\pi/k$. For a given k, the eigenfunctions of the three branches are considered in the coordinates (x, y, z) as the initial conditions. The volume-weighted L_2 norm is measured at $t = 2\pi/\omega(k)$ and defined as follows:

$$\epsilon = \sqrt{\frac{\sum_n \sum_{i,j,k} (\delta Q_{n,i,j,k} - \delta Q_{n,\rm exact}(\boldsymbol{x}_{i,j,k}))^2 \Delta V_{i,j,k}}{\sum_{i,j,k} \Delta V_{i,j,k}}}, \quad (39)$$

where $\boldsymbol{x}_{i,j,k} = (x_i, y_j, z_k)$, $\delta Q_{n,\rm exact}$ represents the exact solution of the nth component of $\delta \boldsymbol{Q}$ at $t = 2\pi/\omega(k)$, and $\Delta V_{i,j,k}$ denotes the volume of the cell centered at $\boldsymbol{x}_{i,j,k}$. We consider the case where $\tilde{c}_{\rm s} = 1/2$ and $\theta = \pi/4$, with the dispersion relation shown in Figure 1.

We compare the results obtained by the four different methods (HLLD, HALL-HLL, HALL-HLLMOD, and HYP-RESIS). For the HYP-RESIS runs, $C_{\rm hyp}$ is fixed to 0.05, because this value provides the minimum dissipation required to eliminate the numerical fluctuations (Sections 3.2 and 3.3).

3.4.1. Uniform Grids

For the uniform grids, we consider three different wavelengths ($kL_{\rm H} = 0.2$, 2, 20), spanning from the ideal MHD regime to the Hall-dominated regime (Figure 1). The convergence test is performed by changing N ($N = 32$, 64, and 128) using $3 \times 3 \times 4$ combination: the three branches, the three different wavelengths, and the four different methods (HLLD, HALL-HLL, HALL-HLLMOD, and HYP-RESIS). The results are summarized in Figure 9.

Both HYP-RESIS and HLLD exhibit second-order convergence across all the branches and wavelengths. The errors for HYP-RESIS and HLLD are nearly identical, indicating that the hyper-resistivity with $C_{\rm hyp} = 0.05$ does not significantly dampen linear waves.

Next, the results of HALL-HLL are compared with those of HLLD. The importance of the Hall effect in the signal speed of the HALL-HLL flux is illustrated in Table 2, which shows that the values of $c_{\rm w}(\Delta x^{-1})/\sqrt{c_{\rm A}^2 + c_{\rm s}^2}$ increase with increasing $kL_{\rm H}$ and N.

For $kL_{\rm H} = 0.2$, the Hall effect does not significantly affect the signal speed of the HALL-HLL flux, since $c_{\rm w}(\Delta x^{-1}) \sim \sqrt{c_{\rm s}^2 + c_{\rm A}^2}$. HALL-HLL exhibits second-order convergence, similar to HYP-RESIS and HLLD, for all branches. In the slow-wave branch, the error ϵ in HALL-HLL is approximately twice as large as that in HLLD, whereas the errors are comparable for the fast-wave and Alfvén-wave branches. This discrepancy arises because the numerical dissipation in HALL-HLL is determined by the phase speed of fast waves.

At larger wavenumbers, $kL_{\rm H} = 2$ and 20, Hall-HLL behaves differently from HYP-RESIS and HLLD, because the signal speeds in the HALL-HLL solver are determined by whistler waves. For the fast-wave branch, HALL-HLL shows second-order convergence, and the errors ϵ are comparable to those of HYP-RESIS and HLLD, because the fast-wave branch corresponds to whistler waves. However, for the Alfvén-wave and slow-wave branches, especially at the largest wavenumber $kL_{\rm H} = 20$, the errors in HALL-HLL are much larger than those of HYP-RESIS and HLLD, and decrease with N at a slower rate than second-order convergence, at least in the range $N \leqslant 128$. This occurs because the HALL-HLL solver incorporates the phase speed of the whistler waves, leading to significant numerical dissipation that dampens the linear waves with phase speeds much smaller than $c_{\rm w}$ (Table 2). Both sound and ion-cyclotron waves are significantly dampened at $kL_{\rm H} = 2$ and 20, as shown in Figure 9.

Figure 9 shows that HALL-HLLMOD significantly improves the dissipative properties of HALL-HLL for the Alfvén-wave and slow-wave branches, and restores second-order convergence. However, the errors ϵ in HALL-HLLMOD are still larger than those in HYP-RESIS. This indicates that HYP-RESIS can capture all MHD linear waves more accurately than both HALL-HLL and HALL-HLLMOD.

We compare the performance of HLLD, HALL-HLLMOD, and HYP-RESIS at the highest resolution, $N = 128$. These calculations are conducted on a single HPE Cray XD2000 node with dual Intel Xeon CPU Max 9480 processors. The calculation using HYP-RESIS is only 3% slower than those using HLLD, indicating that the computational cost of the hyper-resistivity term is negligible. The computational speed of HALL-HLLMOD is about 11% (12%) faster than that of HLLD (HYP-RESIS), since the Riemann solver of HALL-HLLMOD is computationally cheaper than that of the HLLD solver. However, to achieve the desired accuracy in the simulations, the total number of cells required with HYP-RESIS can be reduced by a factor of $2^{3/2} \sim 2.8$ compared to HALL-HLL. In this argument, we use the fact that $\epsilon \propto N^{-2}$ and the errors of HYP-RESIS are about half of those of HALL-HLL (Figure 9).

3.4.2. SMR Grids

In this section, we examine whistler wave propagation in SMR grids to evaluate the effect of mesh refinement on numerical stability and global convergence rates. In this analysis, only the fast-wave branch with $kL_{\rm H} = 20$ is considered.

The root grid resolution is set as $N_{\rm root} \times (N_{\rm root}/2) \times (N_{\rm root}/2)$. Refined grids are introduced in the central region, $0.25L \leqslant x \leqslant 0.75L$ and $0.125L \leqslant y, z \leqslant 0.625L$, with cell sizes reduced to half of the root grid size.

Figure 10 shows the B_ζ maps at $z = L/4$ for HLLD, HYP-RESIS with $C_{\rm hyp} = 0.05$, and HALL-HLL. Unlike uniform grids, numerical instabilities arise in SMR grids. Small-scale waves are excited near the level boundaries and grow over time. Both

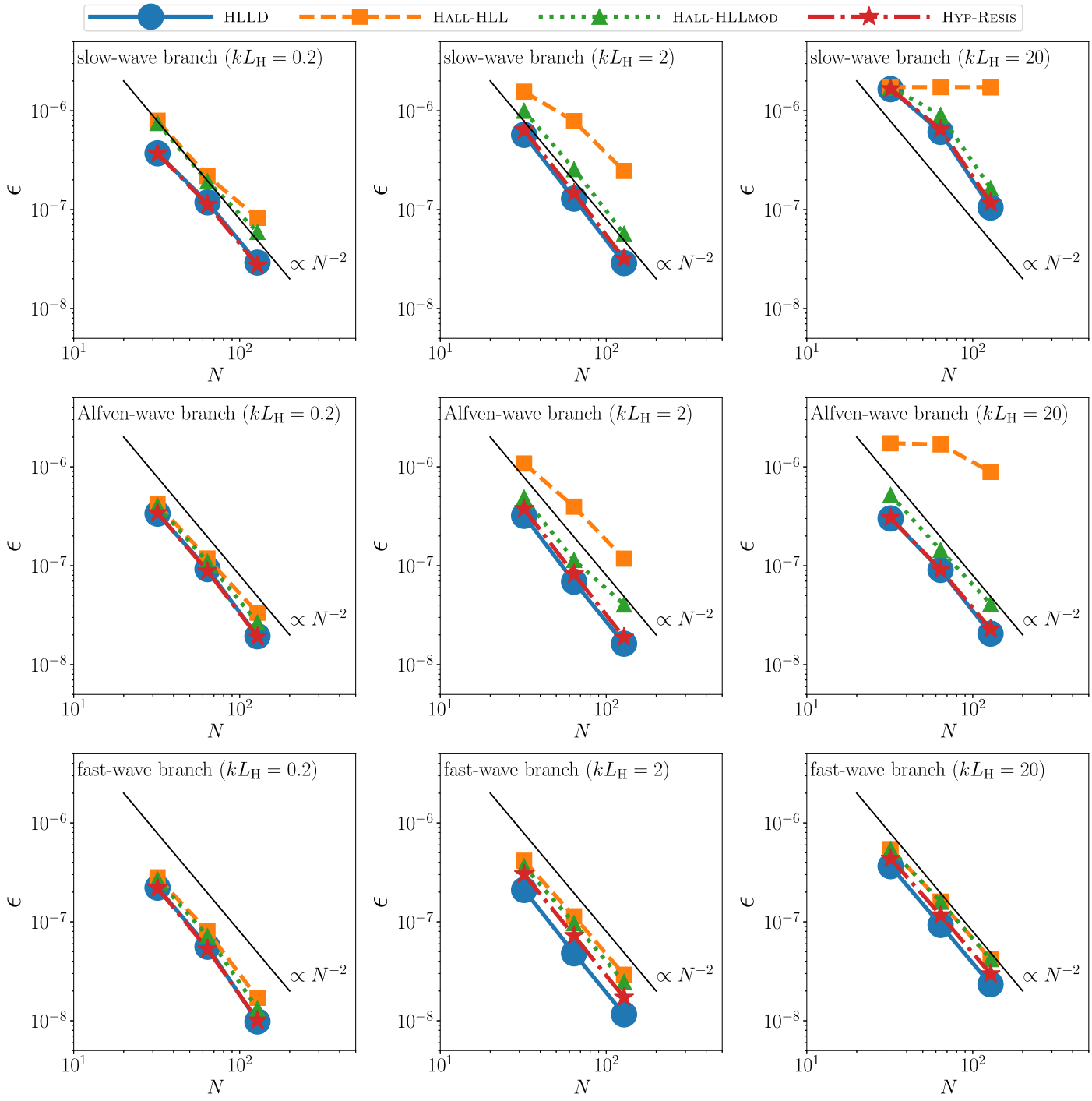

Figure 9. Results of the convergence test ($\bar{c}_s = 1/2$ and $\theta = \pi/4$) for HLLD, Hall-HLL, Hall-HLLmod, and Hyp-Resis with $C_{hyp} = 0.05$. The left, middle, and right columns correspond to the results for $kL_H = 0.2$, $kL_H = 2$, and $kL_H = 20$, respectively. The top, middle, and bottom rows correspond to the slow-wave branch, Alfvén-wave branch, and fast-wave branch, respectively. For reference, the black solid lines proportional to N^{-2} are plotted.

Table 2

The Values of $c_w(k_{max} = \Delta x^{-1})$ Divided by $\sqrt{c_s^2 + c_A^2}$, Which Is the Maximum Value of c_f

kL_H	$N = 32$	$N = 64$	$N = 128$
0.2	1.06	1.25	1.69
2	3.28	6.20	12.2
20	16.9	30.8	121

Hyp-Resis and Hall-HLL produce stable results, as illustrated in Figures 10(b) and (c). A comparison of these panels reveals no significant difference in B_ζ between Hyp-Resis and Hall-HLL.

Figure 11 presents the global convergence rates. Both Hall-HLL and Hyp-Resis demonstrate second-order global convergence. As shown in Figure 9, the errors ϵ are slightly smaller for Hyp-Resis than for Hall-HLL. Furthermore, in each implementation, the SMR grid results in smaller errors compared to the uniform grid, as expected.

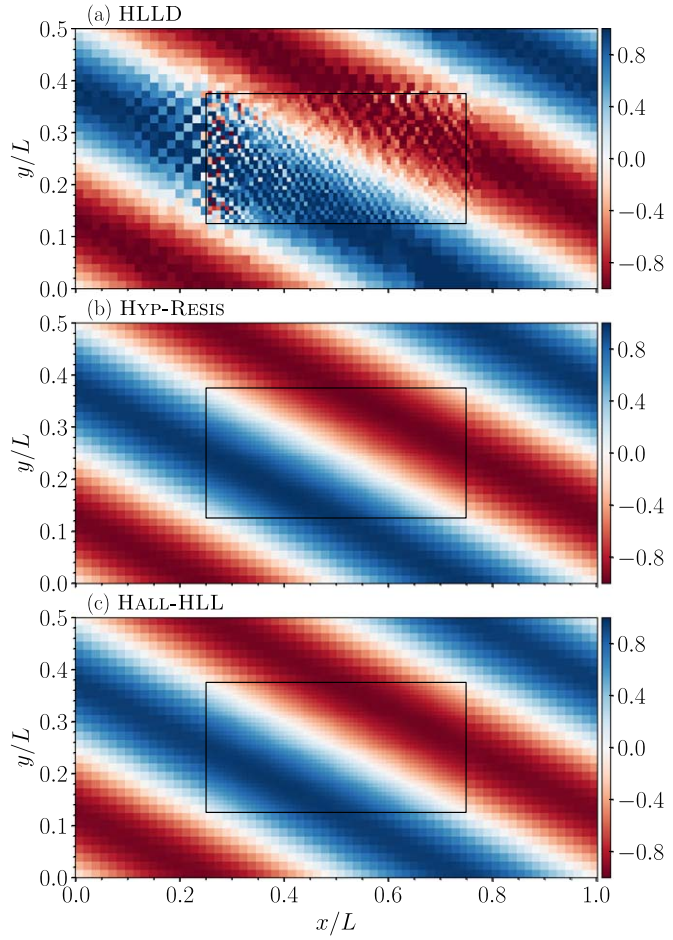

Figure 10. B_ζ maps at the plane $z = L/4$ for (a) HLLD, (b) Hyp-Resis with $C_{\rm hyp} = 0.05$, and (c) Hall-HLL. The snapshots are taken at $t = \pi/\omega(k)$. In each panel, the rectangle encloses the refined region.

3.5. Kelvin–Helmholtz Instability

The Kelvin–Helmholtz (KH) instability in the presence of the Hall effect was investigated by S. P. Talwar & G. L. Kalra (1967) and A. K. Sen & C. K. Chou (1968). Their findings indicate that for super-Alfvénic shear flows, the Hall effect enhances the growth rate. B. P. Pandey (2018) demonstrated that the Hall effect destabilizes sub-Alfvénic shear flows, which are stable under ideal MHD conditions (S. Chandrasekhar 1961).

3.5.1. Predictions from Linear Analyses

Before presenting the numerical setup, we provide a brief overview of the growth rate derived by B. P. Pandey (2018). The unperturbed state consists of a uniform gas with $v_x(y) = \mathcal{M}_{\rm A} c_{\rm A}$ for $y \geqslant 0$ and $v_x(y) = -\mathcal{M}_{\rm A} c_{\rm A}$ for $y < 0$, where $c_{\rm A}$ denotes the Alfvén speed of the unperturbed state, and $\mathcal{M}_{\rm A}$ is the Alfvén Mach number of the shear flow. The magnetic field is uniform and aligned with the shear flow along the x-axis. By considering perturbations in the form $e^{\sigma t + ikx}$, the following dispersion relation is obtained by applying the appropriate boundary conditions (S. P. Talwar & G. L. Kalra 1967; A. K. Sen & C. K. Chou 1968; B. P. Pandey 2018):

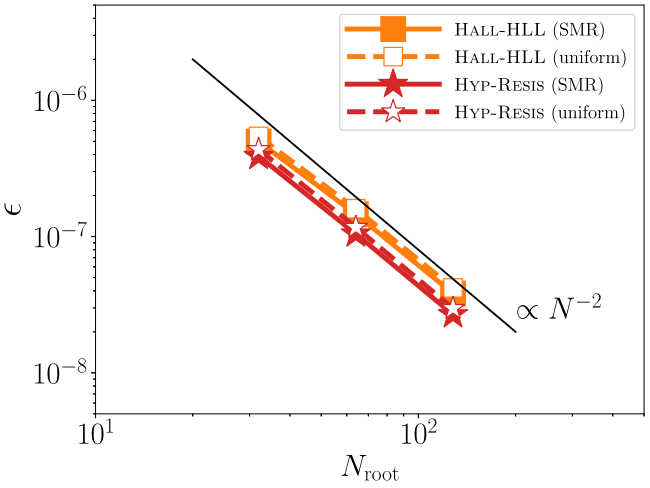

Figure 11. Convergent test of whistler waves with $\tilde{c}_{\rm s} = 1/2$ and $kL_{\rm H} = 20$ for Hall-HLL and Hyp-Resis. The L2 norms measured at $t = 2\pi/\omega(k)$ are plotted as a function of $N_{\rm root}$. For comparison, the results for the uniform grid are shown with dashed lines.

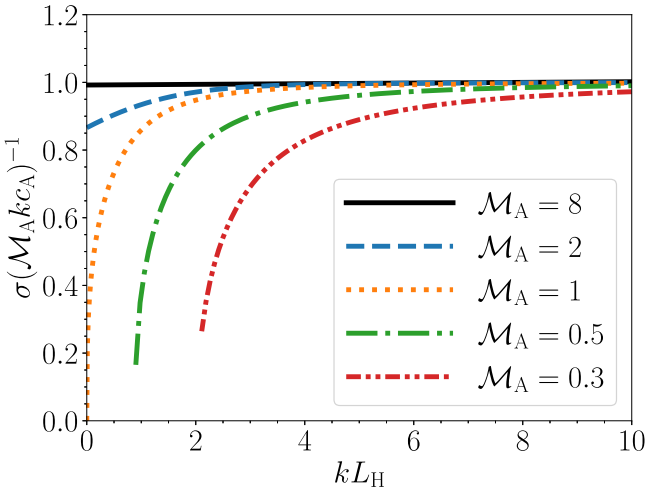

Figure 12. Growth rate of the KH instability as a function of $kL_{\rm H}$ for $\mathcal{M}_{\rm A} = 8$, 2, 1, 0.5, and 0.3.

$$(2 + \tilde{\sigma}_2^2 + \tilde{\sigma}_1^2)\{Q_1\tilde{\sigma}_1(\tilde{\sigma}_2^2 + 1) + Q_2\tilde{\sigma}_2(\tilde{\sigma}_1^2 + 1)\} + kL_{\rm H}(\tilde{\sigma}_2^2 - \tilde{\sigma}_1^2)^2 = 0, \tag{40}$$

where $\tilde{\sigma}_1 = \sigma/(kc_{\rm A}) + i\mathcal{M}_{\rm A}$, $\tilde{\sigma}_2 = \sigma/(kc_{\rm A}) - i\mathcal{M}_{\rm A}$ and

$$Q_j = \sqrt{(\tilde{\sigma}_j kL_{\rm H})^2 + (\tilde{\sigma}_j^2 + 1)^2}\,. \tag{41}$$

Figure 12 shows the growth rate of the purely growing mode, which develops without oscillations, as a function of $kL_{\rm H}$ for various values of $\mathcal{M}_{\rm A}$.

For the Hall-dominated limit ($kL_{\rm H} \gg 1$), Q_j can be approximated as $\tilde{\sigma}_j kL_{\rm H}$. Consequently, Equation (40) becomes independent of $kL_{\rm H}$ and simplifies to:

$$\left\{\left(\frac{\omega}{kc_{\rm A}}\right)^2 + (\mathcal{M}_{\rm A} - 1)^2\right\}\left\{\left(\frac{\omega}{kc_{\rm A}}\right)^2 + (\mathcal{M}_{\rm A} + 1)^2\right\} \times \left(\frac{\omega}{kc_{\rm A}} - \mathcal{M}_{\rm A}\right)\left(\frac{\omega}{kc_{\rm A}} + \mathcal{M}_{\rm A}\right) = 0. \tag{42}$$

Equation (42) has one purely growing mode, given by

$$\sigma_{\rm hall} = kc_{\rm A}\mathcal{M}_{\rm A}. \tag{43}$$

This behavior differs significantly from the ideal MHD case, where sub-Alfvénic shear flows are stabilized by the Lorentz force.

For small values of $kL_{\rm H}$, the properties of σ differ between super- and sub-Alfvénic cases. In the super-Alfvénic regime, at $kL_{\rm H} = 0$, the growth rate is identical to that in ideal MHD:

$$\sigma_{\rm ideal} = kc_{\rm A}\sqrt{\mathcal{M}_{\rm A}^2 - 1} \tag{44}$$

(S. Chandrasekhar 1961). As $kL_{\rm H}$ increases, σ increases and asymptotically approaches $\sigma_{\rm hall}$. Conversely, in the sub-Alfvénic regime, Figure 12 shows that purely growing modes exist only when $kL_{\rm H}$ exceeds a critical value, which is larger for smaller values of $\mathcal{M}_{\rm A}$ (B. P. Pandey 2018).

3.5.2. Numerical Setting

The two-dimensional computational domain is defined as $|x| \leqslant 1/2$ and $|y| \leqslant 1$, and is discretized into 256×512 cells. A uniform gas with density ρ_0 and pressure P_0 is considered. The initial unperturbed gas flow and magnetic field are aligned with the x-axis. To impose periodic boundary conditions in all directions, two initial discontinuities are set at $y = \pm 1/2$. Instead of considering perfect discontinuities in the v_x profile, which is consistent with the unperturbed state in the linear analysis presented above, a smoothed v_x profile is employed, to achieve convergence of results (D. Lecoanet et al. 2016). The unperturbed gas flow is given by

$$v_x(y) = \mathcal{M}_{\rm A}c_{\rm A} \times \left\{\tanh\left(\frac{y+1/2}{w_0}\right) - \tanh\left(\frac{y-1/2}{w_0}\right) - 1\right\}, \tag{45}$$

where $w_0 = 0.1$ is a parameter that controls the smoothness of the profile, and $c_{\rm A} = B_0/\sqrt{4\pi\rho_0}$ is the initial Alfvén speed. To track the time evolution of the initial discontinuities of v_x, we solve a scalar field S governed by the advection equation $\partial S/\partial t + \boldsymbol{v}\cdot\boldsymbol{\nabla}S = 0$. The initial profile of S is given by

$$S(y) = \frac{1}{2}\left\{\tanh\left(\frac{y+1/2}{w_0}\right) - \tanh\left(\frac{y-1/2}{w_0}\right)\right\}. \tag{46}$$

The following perturbation is introduced in the vertical velocity field:

$$v_y(x, y) = \delta v \sin(kx) \times \left\{\exp\left(-\frac{(y+1/2)^2}{w_1^2}\right) + \exp\left(-\frac{(y-1/2)^2}{w_1^2}\right)\right\}, \tag{47}$$

where $\delta v = 0.01$ is the perturbation amplitude, $w_1 = 0.2$ is a parameter showing the spatial extent of the v_y perturbation around the initial discontinuities, and k is the wavenumber and set to 2π. No perturbations are added in other variables.

We consider three different Alfvén Mach numbers: $\mathcal{M}_{\rm A} = 8$, 2, and 0.5. The nondimensional parameter $kL_{\rm H}$ is set to 4. All cases are in the Hall-dominated regime, and the growth rates σ are close to $\sigma_{\rm hall}$ (Equation (43)).

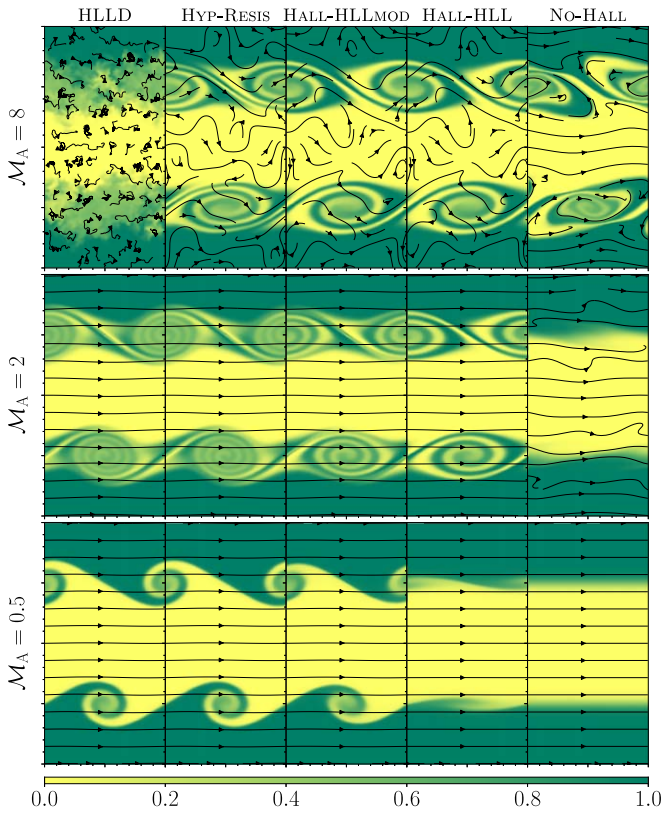

Figure 13. Snapshots of the scalar field S at $t = 4\mathcal{M}_{\rm A}^{-1}$ for $\mathcal{M}_{\rm A} = 0.8$ (top row), $\mathcal{M}_{\rm A} = 2$ (middle row), and $\mathcal{M}_{\rm A} = 0.5$ (bottom row). For each $\mathcal{M}_{\rm A}$, the results of HLLD, Hyp-Resis with $C_{\rm hyp} = 0.05$, Hall-HLLmod, and Hall-HLL are shown from left to right. In the rightmost column, the results without the Hall effect are presented (No-Hall).

3.5.3. Comparison of Different Implementations

Figures 13 and 14 show the $z = 0$ slices of the scalar fields at $t = 4\mathcal{M}_{\rm A}$ and the time evolution of $\delta v_\perp = \sqrt{\langle v_y^2 + v_z^2\rangle}$, respectively.

For reference, the results without the Hall effect, which are labeled "No-Hall," are shown in the rightmost column of Figure 13. Only the $\mathcal{M}_{\rm A} = 0.5$ run without the Hall effect shows a stable result in Figure 13 (also see Figures 14(b), (c), and (d)). This is consistent with the results of the linear analysis by S. Chandrasekhar (1961).

Figure 14(a) shows that for HLLD, the perpendicular velocity dispersions $\delta v_\perp$ with different $\mathcal{M}_{\rm A}$ grow following almost the same lines in the range $\delta v_\perp \lesssim 10^{-2}$ when the time is normalized using the growth rate predicted from Equation (40). Thus, the $\mathcal{M}_{\rm A}$ dependence of the growth rates is consistent with the results of the linear analysis, and the sub-Alfénic case ($\mathcal{M}_{\rm A} = 0.5$) is destabilized by the Hall effect. Note that the growth rates obtained from the simulations are about half the predicted values. This is probably because the settings of the simulations are not exactly the same as those of the linear analysis presented above. For instance, in the simulations, the smoothed profile of the shear flow is considered and the periodic boundary conditions are imposed in all directions.

The results for HLLD are shown in the leftmost panels of Figure 13. Clear rolled-up vortices are seen only for $\mathcal{M}_{\rm A} = 0.5$ and 2, and the magnetic field lines are almost straight in the (x–y) plane. The $\mathcal{M}_{\rm A} = 8$ model suffers from numerical instability due to the Hall effect. This is because strong rolling-

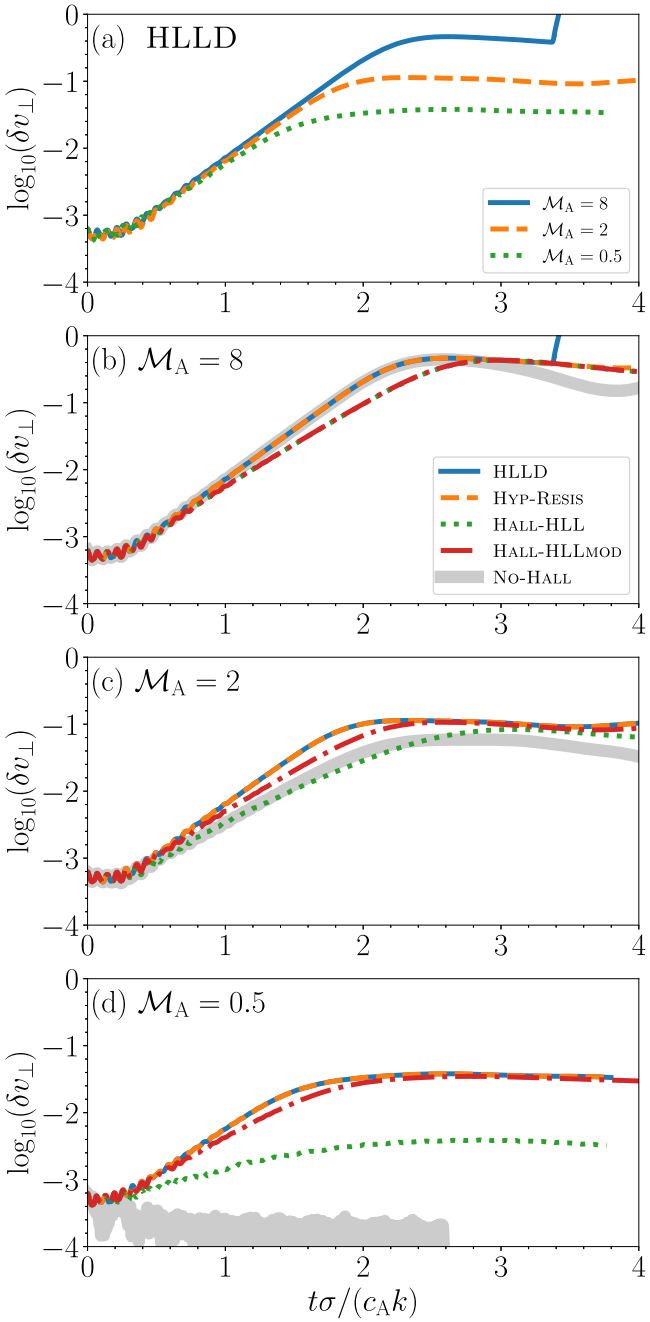

Figure 14. Time evolution of the vertical velocity perturbations $\delta v_\perp = \sqrt{\langle v_y^2 + v_z^2 \rangle}$. The horizontal axis represents the time normalized by $kc_A\sigma^{-1}$ for $kL_H = 4$ and $k = 2\pi$.

up motions bend the magnetic field lines significantly for $\mathcal{M}_A = 8$. The onset of numerical instability is observed as a sudden increase in $\delta v_\perp$ around $t\sigma/(c_A k) \sim 3.4$ in Figure 14(a).

Next, the results for Hyp-Resis with $C_{hyp} = 0.05$ are investigated. For $\mathcal{M}_A = 2$ and 0.5, the S maps are almost identical to those for HLLD. For $\mathcal{M}_A = 8$, the hyper-resistivity suppresses the numerical instability that occurs for HLLD. This feature is quantitatively evident in Figures 14(b)–(d). For all values of $\mathcal{M}_A$, the time evolution of $\delta v_\perp$ for Hyp-Resis is almost identical to that for HLLD except for the numerical instability. This indicates that hyper-resistivity does not introduce significant dissipation.

In contrast, Hall-HLL produces dissipative results, while the amount of numerical dissipation depends on $\mathcal{M}_A$. For $\mathcal{M}_A \geqslant 2$, the results of Hall-HLL show clearly rolled-up vortices, although the number of rotations of the vortex sheet is lower than that for Hyp-Resis (Figure 13). Figures 14(b) and (c) show that large numerical dissipation due to Hall-HLL slows the growth of $\delta v_\perp$ compared to Hyp-Resis. For the sub-Alfvénic case ($\mathcal{M}_A = 0.5$), the development of vortices is strongly suppressed in Figure 13. The linear growth rate and saturation level of $\delta v_\perp$ are both significantly lower for Hall-HLL than those for Hyp-Resis.

These properties of Hall-HLL are consistent with the results of the convergence test in the Hall-dominated regime ($kL_H = 20$) shown in Section 3.4. The development of the KH instability for super-Alfvénic cases is influenced by whistler waves, which are captured reasonably well by Hall-HLL (see the fast-wave branch in Figure 9). However, for sub-Alfvénic cases, ion-cyclotron waves, which are strongly damped by Hall-HLL, play an important role in the development of the KH instability.

In a similar way to Section 3.4, Hall-HLLmod significantly improves the dissipative results of Hall-HLL, especially for smaller $\mathcal{M}_A$. However, Hall-HLLmod produces more dissipative results than Hyp-Resis. We will publicly release our implementation of the Hall effect shortly.

4. Conclusions

In this paper, we evaluate the performance of several numerical methods for the Hall effect found in the literature, which are listed in Table 1, based on an extensive series of test calculations. The Hall effect is implemented in `Athena++` (J. M. Stone et al. 2020; see Section 2.4). Two types of implementations of the Hall effect are considered. One is Hall-HLL, where the phase speed of whistler waves is taken into account to compute the signal speeds in the HLL numerical fluxes (G. Lesur et al. 2014). The modified version of Hall-HLL (Hall-HLLmod) proposed by P. Marchand et al. (2019) is also tested. In Hall-HLLmod, the hydrodynamical variables (the density, momentum, and total energy) are updated by using the original HLL numerical fluxes, whereas the Hall-HLL numerical fluxes are used to update the magnetic field. The other implementation (Hyp-Resis) introduces a fourth-order hyper-resistivity into the induction equation.

An appropriate hyper-resistivity coefficient ($C_{hyp} \sim 0.05$) is determined to ensure both numerical stability and high accuracy based on numerical experiments and the von Neumann stability analysis (Sections 3.2.2, 3.3, and also see the Appendix).

The difference in the performance of the methods is clearly observed in the convergence test of linear waves (see Section 3.4). In the Hall-dominated regime, Hyp-Resis exhibits second-order convergence for all types of Hall-MHD linear waves, and numerical dissipation caused by the hyper-resistivity term does not significantly affect the accuracy of the solutions. By contrast, Hall-HLL shows significantly slower convergence than second order due to numerical dissipation in the ion-cyclotron wave and sound wave, whereas it exhibits second-order convergence for the whistler wave. This occurs because the numerical dissipation in Hall-HLL is determined by the fastest phase speed among the linear waves, which is the whistler wave phase speed. This behavior is also seen in the

KH instability test (Section 3.5). Hall-HLLMOD significantly reduces numerical dissipation compared to Hall-HLL but produces more diffusive results than Hyp-Resis.

Section 3.4.1 demonstrated that Hyp-Resis with $C_{\rm hyp} \sim 0.05$ is also a suitable choice in terms of computational performance. The computational cost of calculating the hyper-resistivity term is negligible compared to the total cost. Hyp-Resis is slightly slower than Hall-HLLMOD for the same resolution, but it can achieve the same accuracy with considerably fewer grid points. In other words, it can achieve better accuracy for the same computational cost.

In summary, hyper-resistivity with an appropriate coefficient ensures both numerical stability and high accuracy, making it the optimal choice for simulating phenomena involving the Hall effect.

Acknowledgments

Numerical computations were carried out on Cray XC50 and XD2000 at the Center for Computational Astrophysics of the National Astronomical Observatory of Japan. This work was supported in part by JSPS KAKENHI Grant Numbers JP21H00056 (K.I.), JP16H05998, JP21H04487, and JP22KK0043 (K.T. and K.I.). This research was also supported by MEXT through the "Program for Promoting Researches on the Supercomputer Fugaku" ("Toward a unified view of the universe: from large scale structures to planets," JPMXP1020200109, and "Structure and Evolution of the Universe Unraveled by Fusion of Simulation and AI," Q10 JPMXP1020230406).

Software: Athena++ (J. M. Stone et al. 2020), numpy (S. van der Walt et al. 2011), Matplotlib (J. D. Hunter 2007).

Appendix
Von Neumann Analysis for Hall-MHD

We present the results of the von Neumann analysis for Hall-MHD. For whistler waves whose wavenumbers satisfy $\eta_{\rm H} k \gg c_{\rm A}$, the ideal term $\boldsymbol{\nabla} \times (\boldsymbol{v} \times \boldsymbol{B})$ is much smaller than the Hall term in the induction equation. In addition, the gas is nearly static, because the velocity perturbations δv are much smaller than $\delta B/\sqrt{4\pi\rho_0}$. Thus, we consider the following induction equation:

$$\frac{\partial \boldsymbol{B}}{\partial t} = -\boldsymbol{\nabla} \times \left(\eta_{\rm H} \frac{(\boldsymbol{\nabla} \times \boldsymbol{B}) \times \boldsymbol{B}}{|\boldsymbol{B}|} \right). \tag{A1}$$

The computational volume is divided into cells with a size of $\Delta x \Delta y \Delta z$. We assume uniform grids, for simplicity. The cell centers are defined at $(i\Delta x, j\Delta y, k\Delta z)$ and the variable Q is denoted as $Q_{i,j,k}$. The magnetic fields are defined at the cell surfaces: $(B_x)_{i-1/2,j,k}$, $(B_y)_{i,j-1/2,k}$, and $(B_z)_{i,j,k-1/2}$.

For the unperturbed state, we consider a static gas with constant density and pressure and a uniform magnetic field of $\boldsymbol{B}_0 = (B_{x0}, B_{y0}, B_{z0})$. A plane wave perturbation with a wavenumber vector of $\boldsymbol{\kappa} = (\kappa_x, \kappa_y, \kappa_z)$ is considered. The magnetic field components are given by:

$$\begin{aligned}
(B_x)_{i-\frac{1}{2},j,k} &= B_{x0} + \delta B_x e^{I(\alpha_x(i-\frac{1}{2})+\alpha_y j+\alpha_z k)}, \\
(B_y)_{i,j-\frac{1}{2},k} &= B_{y0} + \delta B_y e^{I(\alpha_x i+\alpha_y(j-\frac{1}{2})+\alpha_z k)}, \\
(B_z)_{i,j-\frac{1}{2},k} &= B_{z0} + \delta B_z e^{I(\alpha_x i+\alpha_y(j-\frac{1}{2})+\alpha_z k)},
\end{aligned} \tag{A2}$$

where $\alpha_x = \kappa_x \Delta x$, $\alpha_y = \kappa_y \Delta y$, $\alpha_z = \kappa_z \Delta z$, and I is the imaginary unit. Substituting Equation (A2) into the discretized form of Equation (A1), one obtains

$$\frac{\partial \delta \boldsymbol{B}}{\partial t} = \mathcal{R} \delta \boldsymbol{B}, \tag{A3}$$

where $\delta \boldsymbol{B} = (\delta B_x, \delta B_y, \delta B_z)$,

$$\mathcal{R} = 2\eta_{\rm H} C \times \begin{pmatrix} 0 & -\sin(\alpha_z/2)/\Delta z & \sin(\alpha_y/2)/\Delta y \\ \sin(\alpha_z/2)/\Delta z & 0 & -\sin(\alpha_x/2)/\Delta x \\ -\sin(\alpha_y/2)/\Delta y & \sin(\alpha_x/2)/\Delta x & 0 \end{pmatrix}, \tag{A4}$$

and

$$C = 2 \prod_{l=x,y,z} \cos\left(\frac{\alpha_l}{2}\right) \sum_{l=x,y,z} \left[\frac{B_{l0} \tan(\alpha_l/2)}{B_0 \Delta l} \right]. \tag{A5}$$

C is reduced to $\boldsymbol{k} \cdot \boldsymbol{B}/B_0$ in the small-wavenumber limit ($\alpha_l \ll 1$).

With third-order time integrators, one obtains $\delta \boldsymbol{B}^{n+1} = \mathcal{Q} \delta \boldsymbol{B}^n$, where $\mathcal{Q} = \mathcal{I} + \mathcal{R}\Delta t + \mathcal{R}^2 \Delta t^2/2 + \mathcal{R}^3 \Delta t^3/6$. The discrete form is stable if the absolute values of the eigenvalues λ of $\mathcal{Q}$ are less than unity, or

$$|\lambda| = \sqrt{\left(1 - \frac{\xi_{\rm H}^2}{2}\right)^2 + \left(\xi_{\rm H} - \frac{\xi_{\rm H}^3}{6}\right)^2} < 1, \tag{A6}$$

where

$$\xi_{\rm H} = \eta_{\rm H} \Delta t C \sqrt{\sum_{l=x,y,z} \left(\frac{2\sin(\alpha_l/2)}{\Delta l} \right)^2}. \tag{A7}$$

For small-wavenumber limits, Equation (A6) reduces to that derived by M. W. Kunz & G. Lesur (2013; see their Appendix B).

Equation (A6) is reduced to $\xi_{\rm H} < \sqrt{3}$. A conservative criterion for ensuring the stability of any linear wave is

$$\frac{4\sqrt{3}\,\eta_{\rm H} \Delta t}{\min(\Delta x^2, \Delta y^2, \Delta z^2)} < \sqrt{3}, \tag{A8}$$

where we use the fact that $C < 2/\min(\Delta x, \Delta y, \Delta z)$ and $\sin(\alpha_l/2) < 1$.

For second-order time integrators where $\mathcal{Q} = \mathcal{I} + \mathcal{R}\Delta t + \mathcal{R}^2 \Delta t^2/2$, $|\lambda|$ becomes $\sqrt{1 + \xi_{\rm H}^2/4}$, indicating that the discretization form is unconditionally unstable (S. A. E. G. Falle 2003; M. W. Kunz & G. Lesur 2013).

ORCID iDs

Kazunari Iwasaki https://orcid.org/0000-0002-2707-7548
Kengo Tomida https://orcid.org/0000-0001-8105-8113

References

Bai, X.-N. 2014, ApJ, 791, 137
Bai, X.-N., & Stone, J. M. 2017, ApJ, 836, 46
Béthune, W., Lesur, G., & Ferreira, J. 2017, A&A, 600, A75
Birn, J., Drake, J. F., Shay, M. A., et al. 2001, JGR, 106, 3715
Chacón, L., & Knoll, D. A. 2003, JCoPh, 188, 573
Chandrasekhar, S. 1961, Hydrodynamic and Hydromagnetic Stability (Oxford: Clarendon Press)
Collins, D. C., Xu, H., Norman, M. L., Li, H., & Li, S. 2010, ApJS, 186, 308
Davis, S. F. 1988, SISC, 9, 445
Einfeldt, B. 1988, SJNA, 25, 294
Evans, C. R., & Hawley, J. F. 1988, ApJ, 332, 659
Falle, S. A. E. G. 2003, MNRAS, 344, 1210

Fromang, S., Hennebelle, P., & Teyssier, R. 2006, A&A, 457, 371
Gardiner, T. A., & Stone, J. M. 2005, JCoPh, 205, 509
Gardiner, T. A., & Stone, J. M. 2008, JCoPh, 227, 4123
Gottlieb, S., Ketcheson, D. I., & Shu, C.-W. 2009, JSCom, 38, 251
Gourgouliatos, K. N., Kondić, T., Lyutikov, M., & Hollerbach, R. 2015, MNRAS, 453, L93
Hameiri, E., Ishizawa, A., & Ishida, A. 2005, PhPl, 12, 072109
Harten, A., Lax, P. D., & van Leer, B. 1983, SIAMR, 25, 35
Hunter, J. D. 2007, CSE, 9, 90
Kunz, M. W., & Lesur, G. 2013, MNRAS, 434, 2295
Lecoanet, D., McCourt, M., Quataert, E., et al. 2016, MNRAS, 455, 4274
Lesur, G., Kunz, M. W., & Fromang, S. 2014, A&A, 566, A56
Ma, Z. W., & Bhattacharjee, A. 2001, JGR, 106, 3773
Mandt, M. E., Denton, R. E., & Drake, J. F. 1994, GeoRL, 21, 73
Marchand, P., Commerçon, B., & Chabrier, G. 2018, A&A, 619, A37
Marchand, P., Tomida, K., Commerçon, B., & Chabrier, G. 2019, A&A, 631, A66
Mignone, A., Bodo, G., Massaglia, S., et al. 2007, ApJS, 170, 228
Mignone, A., Tzeferacos, P., & Bodo, G. 2010, JCoPh, 229, 5896
Miyoshi, T., & Kusano, K. 2005, JCoPh, 208, 315
O'Sullivan, S., & Downes, T. P. 2006, MNRAS, 366, 1329
O'Sullivan, S., & Downes, T. P. 2007, MNRAS, 376, 1648
Pandey, B. P. 2018, MNRAS, 476, 344
Pandey, B. P., & Wardle, M. 2008, MNRAS, 385, 2269
Sen, A. K., & Chou, C. K. 1968, CaJPh, 46, 2557
Stone, J. M., Tomida, K., White, C. J., & Felker, K. G. 2020, ApJS, 249, 4
Talwar, S. P., & Kalra, G. L. 1967, JPlPh, 1, 145
Tóth, G., Ma, Y., & Gombosi, T. I. 2008, JCoPh, 227, 6967
van der Walt, S., Colbert, S. C., & Varoquaux, G. 2011, CSE, 13, 22
van Leer, B. 1974, JCoPh, 14, 361
Viganò, D., Garcia-Garcia, A., Pons, J. A., Dehman, C., & Graber, V. 2021, CoPhC, 265, 108001
Wood, T. S., Hollerbach, R., & Lyutikov, M. 2014, PhPl, 21, 052110
Zier, O., Mayer, A. C., & Springel, V. 2024, MNRAS, 527, 8355